

Planck intermediate results. XLI. A map of lensing-induced B -modes

Planck Collaboration: P. A. R. Ade⁸², N. Aghanim⁵⁴, M. Ashdown^{64,6}, J. Aumont⁵⁴, C. Baccigalupi⁸¹, A. J. Banday^{91,10}, R. B. Barreiro⁵⁹, N. Bartolo^{30,60}, S. Basak⁸¹, E. Battaner^{92,93}, K. Benabed^{55,90}, A. Benoit-Lévy^{24,55,90}, J.-P. Bernard^{91,10}, M. Bersanelli^{33,47}, P. Bielewicz^{76,10,81}, J. J. Bock^{61,12}, A. Bonaldi⁶², L. Bonavera⁵⁹, J. R. Bond⁹, J. Borrill^{14,86}, F. R. Bouchet^{55,84}, F. Boulanger⁵⁴, C. Burigana^{46,31,48}, R. C. Butler⁴⁶, E. Calabrese⁸⁸, J.-F. Cardoso^{69,1,55}, A. Catalano^{70,67}, H. C. Chiang^{26,7}, P. R. Christensen^{77,35}, D. L. Clements⁵², S. Colombi^{55,90}, L. P. L. Colombo^{23,61}, C. Combet⁷⁰, B. P. Crill^{61,12}, A. Curto^{59,6,64}, F. Cuttaia⁴⁶, L. Danese⁸¹, R. J. Davis⁶², P. de Bernardis³², G. de Zotti^{43,81}, J. Delabrouille¹, C. Dickinson⁶², J. M. Diego⁵⁹, O. Doré^{61,12}, A. Ducout^{55,52}, X. Dupac³⁷, F. Elsner^{24,55,90}, T. A. Enßlin⁷⁴, H. K. Eriksen⁵⁷, F. Finelli^{46,48}, O. Forni^{91,10}, M. Frailis⁴⁵, A. A. Fraisse²⁶, E. Franceschi⁴⁶, S. Galeotta⁴⁵, S. Galli⁶³, K. Ganga¹, T. Ghosh⁵⁴, M. Giard^{91,10}, Y. Giraud-Héraud¹, E. Gjerløw⁵⁷, J. González-Nuevo^{19,59}, K. M. Górski^{61,94}, A. Gruppuso⁴⁶, J. E. Gudmundsson^{89,79,26}, D. L. Harrison^{56,64}, C. Hernández-Monteagudo^{13,74}, D. Herranz⁵⁹, S. R. Hildebrandt^{61,12}, A. Hornstrup¹⁶, W. Hovest⁷⁴, G. Hurier⁵⁴, A. H. Jaffe⁵², W. C. Jones²⁶, E. Keihänen²⁵, R. Keskitalo¹⁴, T. S. Kisner⁷², J. Knoche⁷⁴, L. Knox²⁷, M. Kunz^{17,54,3}, H. Kurki-Suonio^{25,42}, G. Lagache^{5,54}, A. Lähteenmäki^{2,42}, J.-M. Lamarre⁶⁷, A. Lasenby^{6,64}, M. Lattanzi³¹, R. Leonardi⁸, F. Levrier⁶⁷, P. B. Lilje⁵⁷, M. Linden-Vørnle¹⁶, M. López-Caniego^{37,59}, P. M. Lubin²⁸, J. F. Macías-Pérez⁷⁰, B. Maffei⁶², G. Maggio⁴⁵, D. Maino^{33,47}, N. Mandolesi^{46,31}, A. Mangilli^{54,66}, M. Maris⁴⁵, P. G. Martin⁹, E. Martínez-González⁵⁹, S. Masi³², S. Matarrese^{30,60,40}, P. R. Meinhold²⁸, A. Melchiorri^{32,49}, A. Mennella^{33,47}, M. Migliaccio^{56,64}, S. Mitra^{51,61}, M.-A. Miville-Deschênes^{54,9}, A. Moneti⁵⁵, L. Montier^{91,10}, G. Morgante⁴⁶, D. Mortlock⁵², A. Moss⁸³, D. Munshi⁸², J. A. Murphy⁷⁵, P. Naselsky^{78,36}, F. Nati²⁶, P. Natoli^{31,4,46}, C. B. Netterfield²⁰, H. U. Nørgaard-Nielsen¹⁶, D. Novikov⁷³, I. Novikov^{77,73}, L. Pagano^{32,49}, F. Pajot⁵⁴, D. Paoletti^{46,48}, F. Pasian⁴⁵, G. Patanchon¹, O. Perdereau⁶⁶, L. Perotto^{70 *}, V. Pettorino⁴¹, F. Piacentini³², M. Piat¹, E. Pierpaoli²³, E. Pointecouteau^{91,10}, G. Polenta^{4,44}, G. W. Pratt⁶⁸, J. P. Rachen^{21,74}, M. Reinecke⁷⁴, M. Remazeilles^{62,54,1}, C. Renault⁷⁰, A. Renzi^{34,50}, I. Ristorcelli^{91,10}, G. Rocha^{61,12}, C. Rosset¹, M. Rossetti^{33,47}, G. Roudier^{1,67,61}, J. A. Rubiño-Martín^{58,18}, B. Rusholme⁵³, M. Sandri⁴⁶, D. Santos⁷⁰, M. Savelainen^{25,42}, G. Savini⁸⁰, D. Scott²², L. D. Spencer⁸², V. Stolyarov^{6,87,65}, R. Stompor¹, R. Sudiwala⁸², R. Sunyaev^{74,85}, D. Sutton^{56,64}, A.-S. Suur-Uski^{25,42}, J.-F. Sygnet⁵⁵, J. A. Tauber³⁸, L. Terenzi^{39,46}, L. Toffolatti^{19,59,46}, M. Tomasi^{33,47}, M. Tristram⁶⁶, M. Tucci¹⁷, J. Tuovinen¹¹, L. Valenziano⁴⁶, J. Valiviita^{25,42}, B. Van Tent⁷¹, P. Vielva⁵⁹, F. Villa⁴⁶, L. A. Wade⁶¹, B. D. Wandelt^{55,90,29}, I. K. Wehus⁶¹, D. Yvon¹⁵, A. Zacchei⁴⁵, and A. Zonca²⁸

(Affiliations can be found after the references)

May 31, 2022

Abstract

The “ B -modes,” or curl-like component in the polarization of the cosmic microwave background (CMB) is expected to contain a part generated after the CMB photon decoupling. These secondary B -modes are generated from the E -modes through mixing by the gravitational lensing effect of large-scale structure. This lensing-induced B -mode signal is a valuable probe of the dark matter distribution integrated back to the last-scattering surface, with a broad kernel that peaks at $z \simeq 2$. It also constitutes an important contaminant for the extraction of the primary CMB B -modes from inflation. Combining all-sky coverage and high resolution and sensitivity, *Planck* provides accurate nearly all-sky measurements of both the polarization E -mode signal and the integrated mass distribution via the reconstruction of the CMB gravitational lensing. By combining these two data products, we have produced an all-sky template map of the secondary CMB B -modes using a real-space algorithm that minimizes the impact of sky masks. The cross-correlation of this template with an observed (primordial and secondary) B -mode map can be used to measure the lensing B -mode power spectrum at all angular scales. In particular when cross-correlating with the B -mode contribution directly derived from the *Planck* polarization maps, we obtain lensing-induced B -mode power spectrum measurements at a significance of 12σ , which are in agreement with the theoretical expectation derived from the *Planck* best-fit Λ CDM model. This unique nearly all-sky secondary B -mode template, which includes the lensing-induced information from intermediate to small ($10 \leq \ell \leq 1000$) angular scales, is delivered as part of the Planck 2015 public data release. It will be particularly useful for experiments searching for primordial B -modes, such as BICEP2/Keck Array or LiteBIRD, since it will enable an estimate to be made of the secondary (i.e., lensing) contribution to the measured total CMB B -modes.

Key words. Cosmology: observations – cosmic background radiation – Polarization – Gravitational lensing: weak

1. Introduction

Cosmic microwave background (CMB) polarization anisotropies can be decomposed into curl-free E -modes and gradient-free B -modes. In contrast to primordial E -modes, primordial B -modes are sourced only by tensor perturbations (Polnarev 1985; Spergel & Zaldarriaga 1997;

Kamionkowski et al. 1997; Seljak & Zaldarriaga 1997) that can be formed in the pre-decoupling Universe due to an early inflationary phase (Grishchuk 1975; Starobinsky 1979, 1982). Thus, primordial B -modes of the CMB polarization are a direct probe of cosmological inflation (see Guth 1981; Linde 1982, for details on inflationary theory). The measurement of the primordial B -mode power spectrum, which peaks at degree angular scales, is the main target of a plethora of ground-based experiments and satellite proposals. There was great excitement in early 2014 when B -modes at the relevant angular

*Corresponding author: L. Perotto laurence.perotto@lpsc.in2p3.fr

scales detected by the BICEP2 experiment were interpreted as evidence for inflationary gravitational waves (Ade et al. 2014a). Investigating the polarized dust emission in the BICEP2 observation field using the 353-GHz data, *Planck*¹ revealed a higher dust contamination level than expected from pre-*Planck* foreground models (Planck Collaboration Int. XXX 2014). In BICEP2/Keck Array and Planck Collaborations (2015), a joint analysis of the BICEP2/Keck Array data at 100 and 150 GHz and the full-mission *Planck* data (particularly the 353-GHz polarized data) has been conducted. This provides the state-of-the-art constraints on the tensor-to-scalar ratio, r , which is currently consistent with no detection of a primordial B -mode signal. When combined with the limit derived from the temperature data (as discussed in Planck Collaboration XVI 2014 and Planck Collaboration XIII 2016), the current 95 % upper limit is $r < 0.08$, which already rules out some of the simplest inflationary potentials (Planck Collaboration XX 2016). We stand at the threshold of a particularly exciting epoch that is marked by several ongoing or near-future ground-based experimental efforts, based on technology that is sensitive and mature enough to probe the primordial B -modes to theoretically interesting levels.

In addition to the *primordial* contribution, a *secondary* contribution is expected from the post-decoupling distortion of the CMB polarization due to the effect of gravitational lensing (see Lewis & Challinor 2006, for a review of CMB lensing). In particular, the lensing of the primordial CMB polarization E -modes leads to an additional B -mode contribution. The secondary B -mode contribution to the C_{ℓ}^{BB} power spectrum dominates over the primary one at $\ell \gtrsim 150$, even for large values of the tensor-to-scalar ratio, ($r \sim 1$). Thus, it must be corrected for in order to measure the imprint of primordial tensor modes. This correction is generally referred to as “delensing.”

The secondary B -mode power spectrum can be estimated *indirectly* by cross-correlating the total observed B -mode map with a template constructed by combining a tracer of the gravitational potential and an estimate of the primordial E -modes. Using such a cross-correlation approach, the SPTpol team (Hanson et al. 2013) reported the first estimate of the lensing B -mode power spectrum, consisting of a roughly $< 8\sigma$ measurement in the multipole range $300 < \ell < 2750$ using *Herschel*-SPIRE data as the tracer. The POLARBEAR collaboration obtained the first indirect detection of the lensing B -modes that relies on CMB polarization data only, with a significance of 4σ (Ade et al. 2014b). The ACTPol team also reported a lensing B -mode indirect detection with a significance of 3.2σ within its first season data using the Cosmic Infrared Background fluctuations measured by *Planck* as the mass tracer (van Engelen et al. 2015). Finally, using the full mission temperature and polarization data, *Planck* obtained an indirect measurement of the lensing B -mode power spectrum that covers the multipole range $100 < \ell < 2000$, at a significance level of approximately 10σ , as described in Planck Collaboration XV (2016).

At high multipoles where the secondary B -modes fully dominate the primordial ones, a *direct* estimate is possible. The POLARBEAR collaboration reported the first direct measurement (at around 2σ) of the B -mode

power spectrum in the multipole range $500 < \ell < 2100$ (The Polarbear Collaboration: P. A. R. Ade et al. 2014). The SPTpol experiment also made a direct estimate of the lensing B -modes in the range $300 < \ell < 2300$, representing a $> 4\sigma$ detection (Keisler et al. (2015)). Moreover, a non-zero lensing B -mode signal has been found in the BICEP2/Keck Array data with around 7σ significance, by fitting a freely-floating CMB lensing amplitude in the joint analysis with *Planck* data (BICEP2/Keck Array and Planck Collaborations 2015).

For ground-based experiments targeting the detection of primordial B -modes, a precise estimation of the secondary CMB B -mode power spectrum at large and intermediate angular scales is required in order to achieve precise constraints on inflationary models. For such angular scales, the partial sky coverage of these experiments limits the ability to extract the B -mode power spectrum, as well as to reconstruct the lensing potential at large angular scales, therefore making it difficult to separate the primordial and secondary contributions. Thus, such experiments would benefit from a pre-estimated secondary B -mode template, covering angular scales from a few degrees down to sub-degree scales and matching their sky coverage.

The primary goal of this paper is to present an all-sky secondary B -mode template spanning from intermediate to large angular scales, synthesized using the full mission *Planck* data. In Planck Collaboration XV (2016), the lensing B -mode estimate was band-limited to $\ell > 100$, in order to conservatively alleviate any low- ℓ systematic effects. In contrast, here the focus is on improving the reliability at intermediate angular scales ($10 < \ell < 200$). We also extend the lensing B -mode results of Planck Collaboration XV (2016) by producing a lensing B -mode map, by performing extensive characterization and robustness tests of this template map and by discussing its utility for B -mode oriented experiments. This B -mode map is delivered as part of the *Planck* 2015 data release. The outline of this paper is as follows. Section 2 describes the data and simulations that we use. We detail the methodology for the template synthesis in Sect. 3, and validate the lensing B -mode template reconstruction method using simulations in Sect. 4. We present the template we obtain from *Planck* foreground-cleaned data in Sect. 5, and assess its robustness against foreground contamination and the choice of the data to cross-correlate with in Sect. 6. Section 7 addresses the implications of the template for external experiments targeting primordial B -mode searches. We summarize and conclude in Sect. 8.

2. Data and simulations

We use foreground-cleaned CMB temperature and polarization maps derived from the *Planck* satellite full mission frequency channel maps from 30 to 857 GHz in temperature and 30 to 353 GHz in polarization (Planck Collaboration I (2016); Planck Collaboration II (2016); Planck Collaboration III (2016); Planck Collaboration IV (2016); Planck Collaboration V (2016); Planck Collaboration VI (2016); Planck Collaboration VII (2016); Planck Collaboration VIII (2016)). Our main results are based on Stokes I , Q , and U maps constructed using the SMICA component-separation algorithm (Delabrouille et al. 2003) in temperature and polarization simultaneously (Planck Collaboration IX 2016). The maps are at $5'$ resolution in $N_{\text{side}} = 2048$ HEALPix pixelization (Górski et al. 2005).² For the sake of assessing the robustness of our results, we also use foreground-cleaned maps that are produced using

¹*Planck* (<http://www.esa.int/Planck>) is a project of the European Space Agency (ESA) with instruments provided by two scientific consortia funded by ESA member states and led by Principal Investigators from France and Italy, telescope reflectors provided through a collaboration between ESA and a scientific consortium led and funded by Denmark, and additional contributions from NASA (USA).

²<http://healpix.jpl.nasa.gov>

the other *Planck* component-separation methods, namely Commander, NILC, and SEVEM (Planck Collaboration XII 2014; Planck Collaboration IX 2016; Planck Collaboration X 2016). Note that, since the CMB E -mode polarization signal at $\ell < 30$ has no real impact on the lensing B -modes, we use CMB polarization maps that were not high-pass filtered at $\ell = 30$. These maps are part of the *Planck* 2015 data release and can be accessed through the Planck Legacy Archive.³

For our internal lensing potential reconstruction, we prepare a temperature-targeted mask, following the method described in Planck Collaboration XVI (2014). The mask is a combination of an $f_{\text{sky}} \approx 80\%$ Galactic mask that removes the region contaminated by the Galactic thermal dust emission (using the *Planck* 853 GHz channel map), carbon-monoxide (CO) emission lines (Planck Collaboration XIII 2014; Planck Collaboration I 2016), emission from nearby extended galaxies, and a compact object mask that filters out the detected SZ clusters and point sources using the *Planck* Compton y parameter map and the *Planck* catalogues (Planck Collaboration XXVIII 2014; Planck Collaboration XXIX 2014; Planck Collaboration XXII 2016; Planck Collaboration XXVI 2016; Planck Collaboration XXVII 2016). This mask, which is applied to the temperature map at the stage of the lensing extraction, is referred to as the “lensing” mask. For polarization-targeted masks, we use the “confidence” masks defined by the component-separation algorithms (Planck Collaboration IX 2016).

For methodological validation, as well as for the bias correction of the lensing potential at the map level (known as the “mean-field correction”), we use the *Planck* Full Focal Plane simulations, as described in Planck Collaboration XII (2016). In order to account for the final calibration of the *Planck* 2015 data, the CMB component of the simulations has been rescaled as in Planck Collaboration XV (2016).

3. B -mode map reconstruction

3.1. Formalism

The secondary B -modes of CMB polarization arise from a leakage of a small fraction of the E -modes into B -modes due to the polarization remapping induced by the CMB lensing effect. In terms of the polarization spin-2 components $_{\pm 2}P \equiv Q \pm iU$, and at first order in the lensing potential ϕ , the lensing-induced contribution reads

$$_{\pm 2}P^{\text{lens}}(\hat{n}) = \nabla_{\pm 2}P^{\text{prim}}(\hat{n}) \cdot \nabla\phi(\hat{n}), \quad (1)$$

where $_{\pm 2}P^{\text{prim}}(\hat{n})$ are the polarization fields that would be observed in the absence of the lensing effect (Zaldarriaga & Seljak 1998; Lewis & Challinor 2006). Rewriting the secondary polarization fields in terms of the rotationally invariant E - and B -mode fields, so that

$$_{\pm 2}P^{\text{lens}}(\hat{n}) = \nabla \left[\sum_{\ell'm'} \left(E_{\ell'm'}^{\text{prim}} \pm iB_{\ell'm'}^{\text{prim}} \right) _{\pm 2}Y_{\ell'm'} \right] \cdot \nabla\phi(\hat{n}), \quad (2)$$

and considering their spin spherical harmonic coefficients

$$_{\pm 2}P_{\ell m}^{\text{lens}} = \int d\hat{n} \, _{\pm 2}P^{\text{lens}}(\hat{n}) \, _{\pm 2}Y_{\ell m}^*(\hat{n}), \quad (3)$$

one finds that the gradient-free B -mode polarization receives a secondary contribution that depends on the primordial B -modes and the unlensed curl-free E -modes, of the form

$$B_{\ell m}^{\text{lens}} = \frac{1}{2i} \left(_{+2}P_{\ell m}^{\text{lens}} - _{-2}P_{\ell m}^{\text{lens}} \right). \quad (4)$$

3.2. Algorithm

First, we state the assumptions on which our algorithm is based. Since the E -mode amplitude is at least an order of magnitude greater than the primordial B -mode amplitude, the $B_{\ell m}^{\text{lens}}$ contribution that comes from the E -mode remapping largely dominates over the one from the lensing perturbation of the primordial B -modes. From now on, we can safely neglect the latter, consistent with the assumptions in Planck Collaboration XV (2016). We replace the primordial E -modes that appear in Eq. (2) with the total E -modes, $E = E^{\text{prim}} + \delta E$, which amounts to neglecting the second-order contribution to B^{lens} due to δE , i.e., the lensing perturbation of the E -modes themselves.

We then consider pure E polarization fields:

$$_{\pm 2}P^E(\hat{n}) \equiv Q^E(\hat{n}) + iU^E(\hat{n}) \equiv \sum_{\ell m} E_{\ell m} \, _{\pm 2}Y_{\ell m}(\hat{n}), \quad (5)$$

which define pure- E Stokes parameters Q^E, U^E .

Implementing the above assumptions into Eq. (3) and using the definition given in Eq. (5), we build a secondary polarization estimator that has the generic form

$$_{\pm 2}\hat{P}_{\ell m}^{\text{lens}} = \mathcal{B}_{\ell}^{-1} \int d\hat{n} \, \nabla_{\pm 2}\tilde{P}^E(\hat{n}) \cdot \nabla\tilde{\phi}(\hat{n}) \, _{\pm 2}Y_{\ell m}^*(\hat{n}), \quad (6)$$

where $_{\pm 2}\tilde{P}^E$ and $\tilde{\phi}$ are the filtered versions of the pure- E polarization and lensing potential fields, respectively, whereas \mathcal{B}_{ℓ} is a transfer function ensuring that the estimator is unbiased. These quantities are defined below in Sect. 3.3. We finally define secondary CMB B -mode template Stokes maps ($Q^{\text{lens}}(\hat{n}), U^{\text{lens}}(\hat{n})$) by preserving the B -mode contribution in Eq. (6) and transforming back to real space.

In summary, we reconstruct the all-sky B -mode template using a dedicated pipeline that consists of:

- (i) estimation of the deflection field using the filtered reconstructed gravitational potential, $\nabla\tilde{\phi}(\hat{n})$;
- (ii) computation of the gradient of the filtered pure E -mode input maps, $\nabla_{\pm 2}\tilde{P}^E(\hat{n})$;
- (iii) calculation of the analytical transfer function;
- (iv) construction of the template using Eq. (6);
- (v) formation of a secondary B -mode template using Eq. (4).

These steps are further detailed in the remainder of this section.

3.3. Technical implementation

3.3.1. All-sky lensing potential reconstruction

The integrated gravitational potential back to the last-scattering surface, ϕ , is imprinted in the CMB observables due to the remapping caused by the effect of weak lensing. To first order in ϕ , it results in a correlation between the *observed* CMB maps and the gradient of the (*unlensed*) maps. Building upon this property, quadratic estimators have been proposed to extract a lensing potential estimate from the observed map.

³<http://archives.esac.esa.int/pla2>

We reconstruct the lensing potential over a large fraction of the sky using the all-sky quadratic estimator described in Okamoto & Hu (2003), which has been modified in order to deal with cut skies. In Planck Collaboration XV (2016), foreground-contaminated regions are masked out at the stage of the inverse-variance filtering of the input CMB maps, by allocating infinite variance to masked pixels. The reconstructed ϕ is thus null-valued in the pixels inside the analysis mask. For the sake of synthesizing Stokes maps ($Q^{\text{lens}}(\hat{n}), U^{\text{lens}}(\hat{n})$), as described in Sect. 3.2, using such a masked ϕ estimate would induce prohibitive amounts of mode mixing. Thus, we use the METIS method, in which the masked CMB maps are restored to a complete sky coverage, before their ingestion into the quadratic estimator, by means of an inpainting procedure based on the “sparsity” concept (Abrial et al. 2007). Further details are discussed in Perotto et al. (2010), where this method was first described and in Planck Collaboration XVIII (2014), where it was used to perform consistency tests. As a result of this procedure, our lensing reconstruction method provides a ϕ estimate that is effectively inpainted to cover the full sky. To illustrate this property, Fig. 1 shows a Wiener-filtered version of our ϕ estimate reconstructed from the foreground-cleaned temperature map using SMICA and the $f_{\text{sky}} \simeq 80\%$ lensing mask. The map is shown in Galactic coordinates. As well as offering the advantage of minimizing the bias that the mask induces in the ϕ map, referred to as the “mean-field bias,” this allows us to construct the secondary polarization template map using Eq. (6), alleviating the need for further processing steps to account for partial sky coverage. Then, the mask is propagated to the final lensing B -mode products.

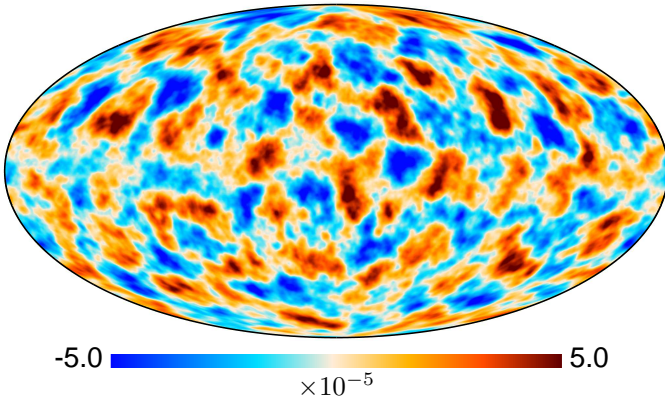


Figure 1. Wiener-filtered lensing potential estimated from the SMICA foreground-cleaned temperature map using the $f_{\text{sky}} \simeq 80\%$ lensing mask. Note that the lensing extraction pipeline we use provides an effective inpainting of the lensing potential, as discussed in Sect. 3.3.1.

The mean-field bias $\langle \bar{\phi}_{LM} \rangle_{\text{MC}}$ is estimated using Monte Carlo (MC) simulations, and is subtracted from the (non-normalized) reconstructed lensing potential $\bar{\phi}$ to obtain the final ϕ estimate, which is

$$\hat{\phi}_{LM} = \mathcal{A}_L (\bar{\phi}_{LM} - \langle \bar{\phi}_{LM} \rangle_{\text{MC}}), \quad (7)$$

where \mathcal{A}_L is the normalization function, which ensures that the estimator is unbiased.⁴ Note that, because the lensed CMB fields are a convolution of the lensing potential and the primary CMB

⁴It is also related to the response function of the quadratic estimator to off-diagonal terms of the CMB covariance \mathcal{R}_L , as defined in equation A.16 of Planck Collaboration XV (2016), via $\mathcal{A}_L = \mathcal{R}_L^{-1}$.

fields, we use multipoles “ L ” for the lensing potential and multipoles “ ℓ ” for CMB fields.

Note that, in addition to the lensing potential quadratic estimate, other tracers of the underlying lensing potential could be used to form a lensing-induced B -mode template. The cosmic infrared background (CIB) emission is expected to be of particular interest for this purpose. In contrast to most of the large-scale structure tracers, which probe only a limited range of redshifts, the redshift distribution of the CIB is predicted to have a broad overlap with the lensing potential kernel (Song et al. 2003). Using the best-fit halo-based model of Planck Collaboration XVIII (2011), Planck Collaboration XVIII (2014) reported a roughly 80% correlation of the CIB fluctuations measured by *Planck* with the lensing potential, in agreement with the model expectations. In Planck Collaboration XV (2016), the CIB fluctuations measured by *Planck* in the 545-GHz channel were used to measure the lensing-induced B -mode power spectrum, finding a significance level only slightly below the measurements employing the lensing potential reconstruction. This determination required a model for the CIB emission in order to calculate its cross-correlation with the lensing potential. However, the uncertainties in the CIB modelling will have a large impact on the lensing B -mode estimate unless the CIB model parameters are marginalized within a joint analysis including lensing cross- and auto-power spectrum measurements of the CIB (Sherwin & Schmittfull 2015). In addition, the foreground residuals are another concern for any lensing B -mode template synthesized from the CIB, as also discussed in Sherwin & Schmittfull (2015). The CIB signal is best measured at high frequencies, where the Galactic dust emission is also important. Any Galactic dust residuals in the CIB template map could be correlated either with the polarized dust residuals or with the intensity-to-polarisation leakage of the dust emission in the CMB E - and B -mode maps. Here we choose to employ only the lensing potential estimate to produce a lensing B -mode template that is model-independent and more robust to foreground residuals. However, it is possible that the CIB could also be used in a future study.

In Planck Collaboration XV (2016), lensing potential reconstructions using either both temperature and polarization data or temperature data only, have been used to derive lensing B -mode power spectrum measurements at roughly the same significance level. In contrast, here we choose not to use the polarization information for the lensing reconstruction, which increases the noise of the ϕ reconstruction by roughly 25%. The reasons for this choice will be discussed in Sect. 4, where we will see that it ensures desirable properties for our template within a B -mode power spectrum measurement, alleviating the need for a Gaussian bias correction, at the price of a marginal increase in uncertainty.

3.3.2. Reconstruction of the secondary polarization fields

Using the lensing potential estimate discussed above and the observed E -mode map, we reconstruct the template of the secondary polarization field as in Eq. (6). To reduce uncertainties we use filtered versions of those maps that are defined as

$$\tilde{\phi}(\hat{n}) = \int d\hat{n} f_L^\phi \hat{\phi}_{LM} Y_{LM}^*(\hat{n}), \quad (8)$$

and

$${}_{\pm 2}\tilde{P}^E(\hat{n}) = \int d\hat{n} f_\ell^E E_{\ell m} {}_{\pm 2}Y_{\ell m}^*(\hat{n}). \quad (9)$$

The filter functions for ϕ and E , f_L^ϕ and f_L^E , are Wiener filters, based on the optimality arguments developed in [Smith et al. \(2009a\)](#). In addition, the ϕ estimate is high-pass filtered to $L \leq 10$ in order to avoid any mean-field residuals. The filtered pure- E polarization fields ${}_{\pm 2}\hat{P}^E$ are directly obtained from the full-sky observed Q and U maps by transforming into the spin-weighted spherical harmonic basis, filtering the E -modes, and reforming Stokes parameter fields with a null B -mode component.

These steps are performed using the fast spin-weighted spherical harmonic transform capability of the HEALPix library to generate Q^E and U^E and compute their derivatives. Thanks to this simple implementation, a B -mode template map at a resolution of $5'$ can be reconstructed from the ϕ estimate and the observed Q and U maps in a reasonable amount of computing time, which enables the use of Monte Carlo simulations. For example, the computing time is about 2 minutes using eight cores of the Linux AMD64 machines of the Institut National de Physique Nucléaire et de Physique des Particules (IN2P3) Computing Center⁵.

3.3.3. Analytical transfer function

Using a harmonic approach, as in [Hu \(2000\)](#), we compute the transfer function that appears in Eq. (6) by imposing the condition that the secondary B -mode template $\hat{B}^{\text{lens}} \equiv ({}_{+2}\hat{P}^{\text{lens}} - {}_{-2}\hat{P}^{\text{lens}})/(2i)$ satisfies

$$\langle B_{\ell m}^* \hat{B}_{\ell' m'}^{\text{lens}} \rangle = \delta_{\ell\ell'} \delta_{mm'} C_{\ell}^{B,\text{fid}}, \quad (10)$$

where $C_{\ell}^{B,\text{fid}}$ is the fiducial lensing-induced B -mode power spectrum ($r = 0$).

In terms of the fiducial power spectra $C_{\ell}^{X,\text{fid}}$, $X = \{E, B, \phi\}$, we obtain a transfer function

$$\mathcal{B}_{\ell} = \frac{1}{C_{\ell}^{B,\text{fid}}} \sum_{L\ell'} f_L^{\phi} C_L^{\phi,\text{fid}} f_{\ell'}^E B_{\ell'} C_{\ell'}^{E,\text{fid}} {}_2F_{\ell L \ell'}, \quad (11)$$

where $B_{\ell'}$ is the beam function of the polarization maps, and ${}_2F_{\ell L \ell'}$ is a geometrical term defined in [Hu \(2000\)](#).

3.3.4. B -mode template synthesis

Our secondary B -mode template is obtained as in Eq. (4), i.e.,

$$\hat{B}_{\ell m}^{\text{lens}} = \frac{1}{2i} ({}_{+2}\hat{P}_{\ell m}^{\text{lens}} - {}_{-2}\hat{P}_{\ell m}^{\text{lens}}). \quad (12)$$

This is obtained from ${}_{\pm 2}\hat{P}_{\ell m}^{\text{lens}}$, the spin-weighted spherical harmonic transforms of our real-space secondary polarization estimates ($Q^{\text{lens}} \pm iU^{\text{lens}}$) that are corrected for the transfer function given in Eq. (11).

4. Validation on simulations

We now validate the pipeline described in Sect. 3 using a Monte Carlo (MC) approach. We analyse our template in cross-correlation with the fiducial polarization, which has two objectives:

- (i) to assess that the template encloses the expected lensing B -mode information, thus validating the assumptions on which the synthesis method relies;

- (ii) to demonstrate its utility for measuring the secondary B -mode power spectrum.

We use the *Planck* Full Focal Plane (FFP) MC temperature and polarization simulation set described in Sect. 2. Specifically, we use 100 FFP I , Q , and U simulations, which include the nine *Planck* frequency CMB and noise realizations that have been processed through the SMICA component-separation method.

4.1. Full-range power spectrum estimate

We apply the pipeline described above to the SMICA I , Q , and U simulations to obtain a set of \hat{B}^{lens} estimates. Then, we form a secondary B -mode cross- C_{ℓ} estimate by cross-correlating \hat{B}^{lens} and the fiducial B -modes using

$$\hat{C}_{\ell}^{BB^{\text{lens}}} = \frac{1}{f_{\text{sky}}^{\text{eff}}(2\ell + 1)} \sum_m B_{\ell m}^* \tilde{B}_{\ell m}^{\text{lens}}, \quad (13)$$

where $\tilde{B}_{\ell m}^{\text{lens}}$ is a shorthand notation for the harmonic coefficients of the apodized version of \hat{B}^{lens} and $f_{\text{sky}}^{\text{eff}}$ is the effective available sky fraction. Note that $\hat{C}_{\ell}^{BB^{\text{lens}}}$ consists of a direct estimator of the secondary B -mode power spectrum, which does not require any noise term subtraction. We estimate the secondary B -mode band-powers by multiplying by $\ell(\ell + 1)/2\pi$ and averaging the multipoles over bins of width $\Delta\ell \geq 100$ in order to further reduce the pseudo- C_{ℓ} multipole mixing.

As a first test, we study the impact of inpainting the masked temperature map from which the lensing potential is extracted. The performance of inpainting methods has been thoroughly assessed in the framework of the lensing potential reconstruction ([Perotto et al. 2010](#); [Benoit-Lévy et al. 2013](#); [Planck Collaboration XVI 2014](#)). In particular, [Benoit-Lévy et al. \(2013\)](#) found that treating the point source mask using an inpainting method based on Gaussian constrained simulations induces a negligible bias on the lensing potential power spectrum estimate after a simple rescaling by the available sky fraction. We obtain similar results when filling in the point source mask using sparse inpainting. However, the lensing signal is not well reconstructed inside large masked regions, such as those contaminated by the Galaxy or the extended sources, as discussed in [Perotto et al. \(2010\)](#), [Plaszczynski et al. \(2012\)](#), and [Planck Collaboration XVI \(2014\)](#). As a consequence, the temperature-targeted mask for the diffuse emission and extended compact sources has to also be applied to the B -mode template map. In addition, we find that the edges of the masked regions also show some contamination. The amount of the contamination and the size of the affected area depend on the size of the masked regions, going from a negligible effect for holes below $30'$ in diameter to a leakage extending over about 1° for large sky cuts (e.g., the Galactic mask). We find that enlarging the mask beyond the border or using a large apodization solves this issue. We conservatively choose to extend the Galactic mask 3° beyond the boundaries and the extended compact object mask (i.e., holes of radial size between 30 and $100'$) $30'$ beyond. We further use cosine apodizations that smoothly go from zero to one over a distance of 2° from the Galactic mask border and over $30'$ from the extended compact source mask border, in order to mitigate the mode mixing. We use the baseline 80 % temperature-targeted mask described in Sect. 2 when performing the lensing reconstruction, then propagate it after enlargement and apodization to the B -mode cross-power spectrum estimation. We observe a negligible residual bias ($\lesssim 1\%$ of the fiducial model compared to the roughly 10 % precision of

⁵<http://cc.in2p3.fr/?lang=en>

the measurements) in the determination of the lensing B -mode power spectrum up to multipoles of 2000.

In a second series of tests, we focus on optimizing the inpainting mask. The mask enlargement efficiently treats the leakage-related bias at the price of a reduction of the available sky; this can be important for weakly connected masks, such as the extended compact source mask. In order to preserve a sufficiently large sky fraction, we choose to reduce our conservative extended compact source mask by removing from the mask any regions that are not masked out by the SMICA temperature confidence mask, i.e., the area that is well-cleaned using the SMICA method. This results in a 25 % reduction of the extended compact source mask. In Sect. 6, we test that our results are consistent whether the extended compact sources are masked out using the optimized or the conservative mask. Our fiducial lensing B -mode mask consists of the combination of the Galactic mask and the optimized extended compact source mask, and preserves about 80 % of the sky. After enlargement as described above, it still retains about 70 % of the sky and is referred to as the “L70” mask.

The averaged $C_\ell^{BB\text{B}^{\text{lens}}}$ band-powers obtained using the L70 mask are presented in Fig. 2. The statistical scatter (standard deviation) within our simulation set provides error bar estimates. In order to isolate the impact of the inpainting, we also perform the lensing B -mode estimation for the lensing potential reconstructed from the full-sky temperature map. The averaged lensing B -mode band-power residuals, i.e., $\Delta C_b^{BB\text{B}^{\text{lens}}} = \sum_{\ell \in b} C_\ell^{BB\text{B}^{\text{lens}}} - C_\ell^{BB\text{B}^{\text{fid}}}$, are plotted in the lower panel of Fig. 2, showing a negligible residual bias of $\lesssim 0.1 \sigma$, which corresponds to $\lesssim 1 \%$ of the power in the fiducial model.

It is worth noting that the choice of extracting the lensing potential from the temperature-only data ensures the absence of Gaussian $N_L^{(0)}$ -like bias, which must be corrected for in the case of a lensing extraction using B -mode information. It also gives a strong suppression of any higher-order bias terms.

4.2. Statistical error budget

We quantify the statistical error associated with our lensing B -mode band-power measure using the scatter of our MC band-power estimates. These MC error bars are compared to semi-analytical errors evaluated following the Gaussian variance prescription (see e.g., Knox 1995),

$$\sigma^2(C_\ell^{BB\text{B}^{\text{lens}}}) = \frac{1}{f_{\text{sky}}^{\text{eff}}(2\ell+1)\Delta\ell} \left[(C_\ell^B)^2 + (C_\ell^B + B_\ell^{-2}N_\ell^B)(\hat{C}_\ell^{B^{\text{lens}}}) \right], \quad (14)$$

where C_ℓ^B and N_ℓ^B are here the MC fiducial signal and noise power spectra, B_ℓ , the beam function, and $\hat{C}_\ell^{B^{\text{lens}}}$ the averaged lensing B -mode template map auto-power spectrum. In principle, the Gaussian variance prescription is not expected to rigorously apply to the lensing B -mode power spectrum estimate, because of its “sub-structure,” since it is based on the sum of the $TTEB$ trispectrum of the observed CMB signal. However, at the Planck polarization noise level, the higher-order terms that enter the variance are subdominant. In addition, the choice to average the $C_\ell^{BB\text{B}^{\text{lens}}}$ estimate over large multipole bins of width $\Delta\ell \geq 100$ further central-limit drives our band-power estimates close to a normal distribution.

In Fig. 3, we plot the MC error bars, as well as the semi-analytical ones. For comparison purposes, we also show the errors one would have obtained from a direct C_ℓ^{BB} measurement by computing the auto-power spectrum of the fiducial B map.

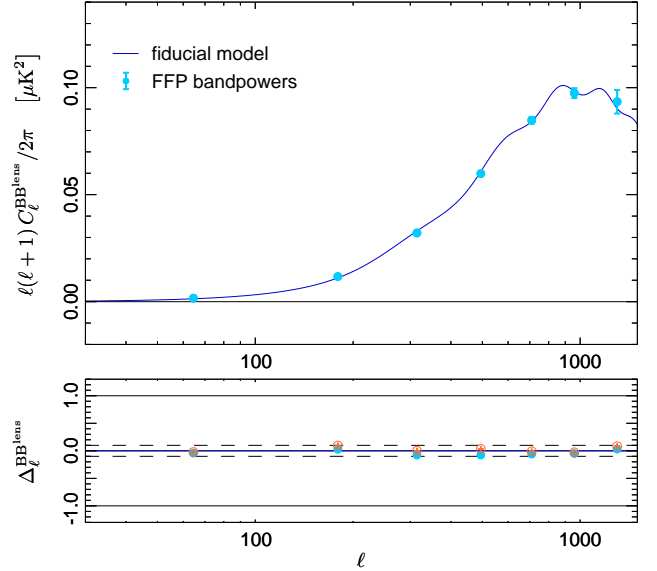


Figure 2. Cross-correlation of the B^{lens} templates with the fiducial B maps in simulations. *Top*: the averaged $C_\ell^{BB\text{B}^{\text{lens}}}$ band-powers (blue points) in multipole bins of $\Delta\ell \geq 100$, with MC scatter error bars using 100 FFP simulations and a mask preserving an effective sky fraction of 65 %. The dark blue curve is the fiducial B -mode power spectrum of our simulations, which assumes $r = 0$. *Bottom*: binned $C_\ell^{BB\text{B}^{\text{lens}}}$ band-powers bias with respect to the fiducial power spectrum, given in units of the 1σ error of a single realization. Dashed lines show the $\pm 1 \sigma$ range of 100 realizations, indicating the precision level to which we are able to test against bias.

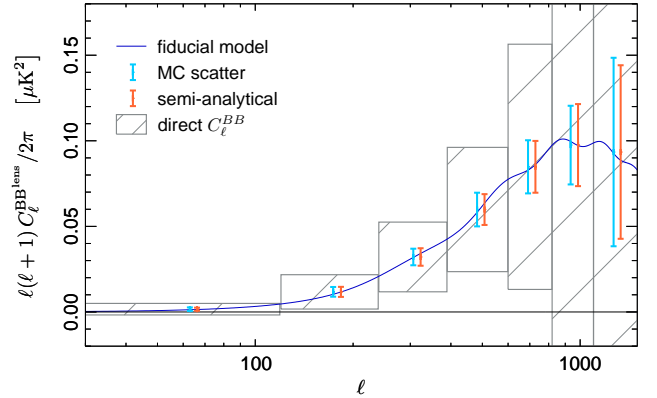


Figure 3. Error budget. We compare the Monte Carlo (MC) derived uncertainties (blue error bars) associated with the cross- C_ℓ B -mode measurements to the semi-analytical ones derived from the Gaussian variance prescription (red). For illustration, we also show the expected sensitivity of the Planck SMICA CMB polarization map to the *direct* auto- C_ℓ B -mode power spectrum (grey boxes), whose uncertainties are a factor of 4 larger than those of our *indirect* cross- C_ℓ using the lensing B -mode template.

The uncertainties in our lensing C_ℓ^B band-powers are well approximated by the Gaussian error estimates at all multipoles. More precisely, the Gaussian prescription leads to 19 % error underestimation in the first multipole bin and less than 10 % underestimation at higher multipoles. These results legitimize the use of the Gaussian error prescription to evaluate uncertainties

in the data. We also find that the uncertainties of our lensing B -mode cross- C_ℓ using the template map are approximately 4 times lower than those of a total B -mode auto- C_ℓ measurement coming directly from the B -mode map.

Gathering the results of our MC analysis, we observe that, when used in cross-correlation with the B -mode map, the lensing B -mode template we compute provides a lensing C_ℓ^B measurement, which: (i) does not rely on any bias subtraction; (ii) has nearly optimal uncertainty; and (iii) has 4 times lower uncertainty than the direct auto- C_ℓ measurement on the fiducial B -mode map.

5. Planck-derived secondary B -mode template

We produce the template map of the lensing B -modes by applying the pipeline described in Sect. 3 to the foreground-cleaned temperature and polarization maps obtained using the SMICA component-separation method, as described in Sect. 2. We first obtain the \hat{Q}^{lens} and \hat{U}^{lens} templates defined in Sect. 3.2, filtered versions of which are plotted in Fig. 4. Specifically, the maps have been smoothed using a Gaussian beam of 1° FWHM in order to highlight any low- ℓ systematic effects, such as those due to intensity-to-polarization leakage. This first inspection indicates that these templates are not affected by any obvious low- ℓ systematic effects. This robustness will be further assessed in Sect. 6 by means of consistency tests using intensity-to-polarization leakage corrected maps.

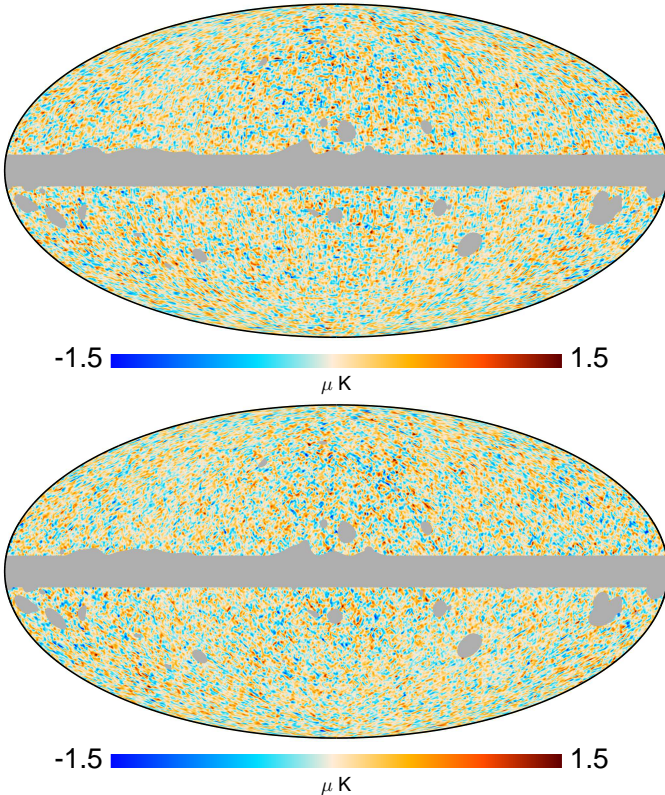


Figure 4. SMICA lensing-induced Q and U templates that have been convolved with a Gaussian beam of $60'$ FWHM in order to highlight structure at large scales ($\ell < 200$ say). No spurious patterns are seen at large angular scales; this represents a basic test of our template's robustness to low- ℓ systematic effects, as further assessed in Sect. 6.

Then we use the SMICA \hat{Q}^{lens} and \hat{U}^{lens} templates to make our secondary B -mode template, as described in Sect. 3.3.4. For illustration purposes, we produced a B -mode template map by inverting $\hat{B}_{\ell m}^{\text{lens}}$ back to pixel-space through an inverse spherical harmonic transform. Whereas our B -mode template contains information in the multipole range $10 < \ell < 2000$, Fig. 5 shows two filtered versions of the B -mode map in order to highlight different ranges of angular scale. The high-resolution map (which is simply slightly smoothed using a Gaussian beam of $10'$ FWHM) should show any important foreground contamination at small angular scales, whereas the low-resolution one (which is smoothed using a 1° Gaussian beam and downgraded to $N_{\text{side}} = 256$ HEALPix resolution) should reveal any large angular scale systematic effects. The fact that there is no evidence for such artefacts in either of the maps plotted in Fig. 5 yields a first indication of the robustness of our template against instrumental and astrophysical systematic effects. Section 6 is devoted to assessing this robustness by means of a series of tests at the power spectrum level, based on measuring the correlation of our template with observed data.

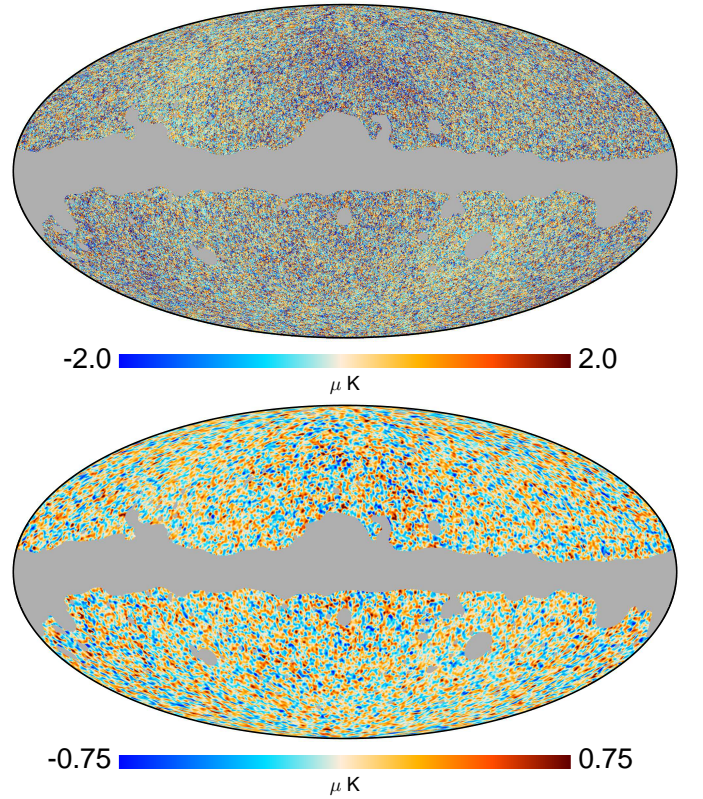


Figure 5. Planck-derived B -mode template map computed using the SMICA foreground-cleaned CMB maps. For illustration, the map has been convolved with a Gaussian beam of $10'$ (upper panel) and $60'$ (lower panel) FWHM. The grey area represents the $f_{\text{sky}} \simeq 80\%$ mask that was used at the lensing potential reconstruction stage. Note that the high-resolution map does not show any foreground residuals, and the low-resolution one shows no evidence for low- ℓ systematic effects, as discussed in Sect. 5.

6. Robustness tests of our template

We now perform a series of consistency tests in order to characterize the B -mode template described in Sect. 5, with a view to using it for measuring the lensing C_ℓ^B in cross-correlation with observed polarization maps. First, we assess the template robustness against foreground residuals. With that aim, we check the stability of our measurement against the use of various masks, and compare the measurements using foreground-cleaned CMB maps obtained with four independent component-separation algorithms. We also use *Planck* polarization maps in different frequency channels in order to assess the stability of the lensing C_ℓ^B estimates with respect to the observed map to which our template is correlated. Finally, we test the consistency of the *Planck* lensing C_ℓ^B measurements obtained using the B -mode template presented in this paper by comparing it to external measurements.

Note that the baseline lensing B -mode power spectrum presented here is consistent with the independent determination of *Planck* Collaboration XV (2016) over the $100 < \ell < 2000$ multipole range, which provides us with further validation of our methodology choices.⁶

6.1. Robustness against foreground residuals

The inspection of the lensing B -mode data product at the map level, discussed in Sect. 5, has not revealed any obvious foreground contamination. Here we further test against foreground systematic effects at the power spectrum level. Cross-correlating the B -mode template with the SMICA foreground-cleaned polarization map, we estimate the lensing C_ℓ^B band-powers using the pseudo- C_ℓ approach described in Sect. 4.1, which we previously used to validate our pipeline.

Our baseline lensing B -mode band-power estimates are obtained using the L70 mask, which leaves approximately 70 % of the sky for analysis. As described in Sect. 4.1, this mask is produced by enlarging the 80 % lensing mask, from which the temperature map is inpainted, in order to alleviate any mask leakage.

6.1.1. Galactic contamination tests

We test against residual foreground contamination around the Galactic plane by comparing the L70 lensing B -mode estimate to estimates using more conservative and more aggressive Galactic masks. The conservative mask L60 consists of the combination of the L70 mask and a larger Galactic mask. The latter is obtained by thresholding the temperature map at 857 GHz to preserve 60 % the sky. The aggressive mask is obtained from the 80 % inpainting mask with no extra enlargement. However, in this case we use a slightly larger apodization that stretches to 3° from the Galactic cut border (instead of 2°) and to 1° from the extended compact object mask border (instead of $30'$). The lensing C_ℓ^B band-power estimates using the L60, L70, and L80 masks are shown in Fig. 6. They are in good agreement, well

within the error bars. In particular, the agreement between the L60 and L70 lensing B -mode estimates indicates that any impact of Galactic foreground residuals lies well below the uncertainties. In addition, the consistency between the L70 and L80 estimates further indicates that: (i) an 80 % Galactic cut suffices to avoid any Galactic foreground residuals in the SMICA map; and (ii) any leakage near the border of the mask (treated by inpainting) has negligible impact.

6.1.2. Extended compact source contamination tests

We test against any residuals due to insufficiently masked extended compact sources. For this purpose, we consider the case of a more conservative masking of the extended compact sources. Namely, we use the union of the 80 % lensing mask described in Sect. 2 and the “confidence” mask of the SMICA temperature map described in *Planck* Collaboration IX (2016). Before the lensing potential extraction, the SMICA temperature map is inpainted for this mask. Then, the lensing B -mode template is masked employing the union of the L70 and SMICA masks, which is labelled “L70s.” The lensing B -mode band-power estimates using this mask are plotted in Fig. 6. The L70s and L70 estimates are in agreement, within uncertainties. This validates our baseline extended compact object mask, the optimization of which has been discussed in Sect. 4.

6.1.3. Polarized foreground emission tests

We test against polarized foreground residuals by combining our temperature-targeted L70 mask with a polarization-targeted mask to form a new mask labelled “L70p.” As a polarization mask, we use the union of the confidence polarization masks provided for the four *Planck* component-separation algorithms (*Planck* Collaboration IX 2016). The lensing B -mode band-power estimates from the L70 and L70p masks are plotted in Fig. 6. The L70p estimate is found to be in agreement with the L70 estimate. We therefore expect no significant bias related to polarized foreground residuals.

We further test the consistency of our band-power estimates by fitting an amplitude with respect to the theoretical C_ℓ^B band-powers. The band-power errors are estimated using the semi-analytical Gaussian variance, Eq. 14, which provides a good approximation, as discussed in Sect. 4.2. In Table 1 we list the fitted amplitudes from our eight multipole bins, corresponding to the range $\ell = 10$ –2000. Whatever the mask used, we find our band-powers to be in good agreement with the expected band-powers computed from the theoretical C_ℓ^B . The fact that all our band-powers, from the most conservative $f_{\text{sky}} = 0.58$ to the most optimistic $f_{\text{sky}} = 0.77$ analysis and whatever the morphology of the mask, are in good agreement, provides an indication of the robustness of the secondary B -mode template against any foreground contamination or any impact of the sky-cut. We judge that the lensing C_ℓ^B measurements are reliable for up to 70 % of the sky.

We further test our template robustness against foreground residuals by comparing results using the four *Planck* component-separation methods, as described in *Planck* Collaboration IX (2016). We focus on the *polarized* foreground residuals; we use different foreground-cleaned Stokes parameter maps, but the same temperature map, specifically the lensing B -mode templates are synthesized from the foreground-cleaned Stokes Q and U maps using different codes and a *fixed* lensing potential extraction using SMICA. We use a common mask that combines

⁶In *Planck* Collaboration XV (2016), one of the null tests conducted for checking the robustness of the lensing potential power spectrum showed mild evidence of a difference from zero, specifically a non-zero signal was seen in the TT curl-mode power spectrum (which contains the $TTTT$ curl-mode trispectrum) with a significance above 2σ . This feature, however, has no real impact in the lensing-induced power spectrum being tested here. First, it contains the $TTEB$ trispectrum, which differs from the trispectrum affected by the curl-mode null-test failure. Additionally, any impact on the variance of the lensing-induced B -mode power spectrum, via some $TTTT$ trispectrum dependent terms, would be totally overwhelmed by the dominant Gaussian noise term.

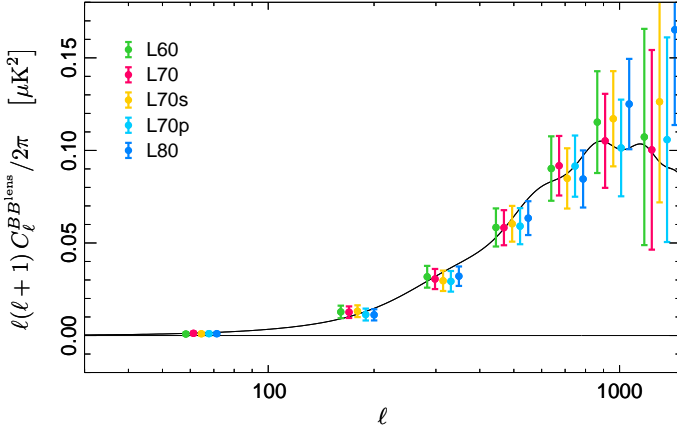


Figure 6. Cross-correlation of our B -mode template with the SMICA polarization map using masks of different levels of conservatism. The data points show our lensing C_ℓ^B band-powers estimated using masks that preserve a sky fraction of 60 % (labelled “L60”), 70 % (“L70”), and 80 % (“L80”), and that are targeted to the foreground emission in temperature, as well as using the 68 % polarization-targeted “L70p” mask and the 68 % “L70s” mask, which gives a more conservative masking of the point sources (see text). The good agreement provides a robustness test against foregrounds, as discussed in Sect. 6.1.

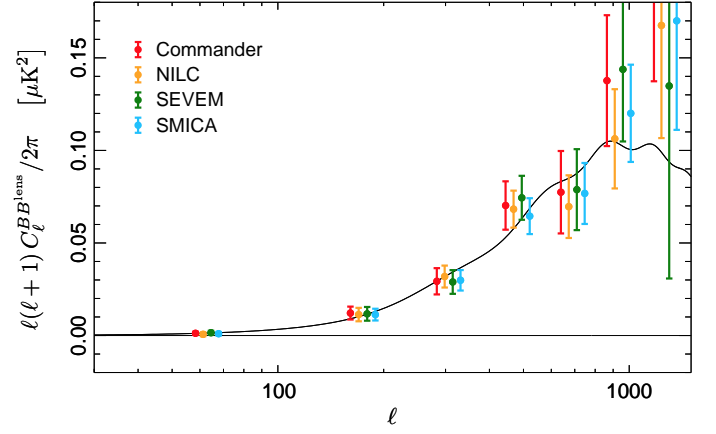


Figure 7. Consistency of our results using the four *Planck* component-separation algorithms. The data points present the lensing B -mode band-power measurements obtained by cross-correlating the lensing B -mode template estimates using the Commander (dark green), NILC (blue), SEVEM (red), and SMICA (yellow) cleaned polarization map with the corresponding B -mode map. The four estimates are quite consistent, as discussed in Sect. 6.1, strongly indicating the robustness of our baseline template against polarized foreground residuals.

Table 1. Band-power amplitudes for various analysis masks, which are listed in the first column. The columns labelled “ f_{sky} ” and “ $f_{\text{sky}}^{\text{eff}}$ ” give the sky fractions that are preserved by the masks and their apodized versions, respectively. The measured band-power amplitudes are given in the column labelled “ $A_{B\text{lens}}$,” and the corresponding B -lensing detection significance levels in the column labelled “S/N.”

Mask label	f_{sky}	$f_{\text{sky}}^{\text{eff}}$	$A_{B\text{lens}}$	S/N
L60	0.58	0.54	0.98 ± 0.09	11.1
L70	0.69	0.65	0.96 ± 0.08	11.9
L70p	0.68	0.64	0.94 ± 0.08	11.3
L70s	0.68	0.61	0.97 ± 0.08	11.8
L80	0.77	0.69	1.00 ± 0.08	12.8

our SMICA lensing Galactic mask and the union polarization mask discussed in Planck Collaboration IX (2016). Fig. 7 shows the resulting lensing B -mode power spectra, obtained through cross-correlation of the lensing B -mode templates with the input Stokes Q and U maps from the corresponding codes.

The four Stokes Q and U foreground-cleaned solutions lead to consistent lensing B -mode power spectrum measurements (within 1σ) over the entire multipole range probed. We measure fits to the amplitude with respect to the fiducial model of:

$$\begin{aligned}
 A_{B\text{lens}} &= 1.01 \pm 0.11 \quad (\text{Commander}); \\
 A_{B\text{lens}} &= 0.97 \pm 0.09 \quad (\text{NILC}); \\
 A_{B\text{lens}} &= 1.00 \pm 0.10 \quad (\text{SEVEM}), \\
 A_{B\text{lens}} &= 0.97 \pm 0.08 \quad (\text{SMICA}).
 \end{aligned}$$

These correspond to 9.5σ , 11.3σ , 9.7σ , and 11.8σ detections of the secondary B -modes, respectively. The consistency of the lensing C_ℓ^B measurements based on four CMB solutions with dif-

ferent foreground residuals indicates the immunity of our baseline lensing B -mode template to polarized foreground emission.

6.2. Stability with respect to the observed polarization

So far, we have considered the cross-correlation of the B -mode template synthesized from the Stokes I , Q , and U cleaned maps, with the same Q , U cleaned maps. We now test the cross-correlation of our baseline template with other CMB foreground-cleaned polarization maps. In particular, we use foreground and intensity-to-polarization leakage-corrected *Planck* channel maps at 100, 143, and 217 GHz, which also serve to test the robustness of our template against low- ℓ systematic effects.

In Fig. 8, we compare our fiducial $C_\ell^{BB\text{lens}}$ band-powers from the L70 SMICA analysis to the band-powers obtained by correlating our SMICA B -mode template with polarization maps at 100, 143, and 217 GHz using the same L70 mask. The band-power estimates are in good agreement with each other within uncertainties, indicating the robustness of our template against polarization systematic effects (that mainly affect the low multipoles). We find that our lensing B -mode template provides stable measurements of the CMB lensing B -modes independent of the choice of the polarization maps with which it is correlated.

6.3. Consistency with external results

Our $C_\ell^{BB\text{lens}}$ band-power estimates are a measurement of the lensing B -mode power spectrum that we now compare to measurements reported by other experiments.

The available BB measurements come in two flavours. The B -mode power spectrum can be measured directly from the observed polarization maps, e.g., the BICEP2/Keck Array⁷ combined measurements as reported in BICEP2 and Keck Array Collaborations et al. (2015a). At roughly $\ell > 300$, where the primordial contribution

⁷http://bicepkeck.org/keck_2015_release.html

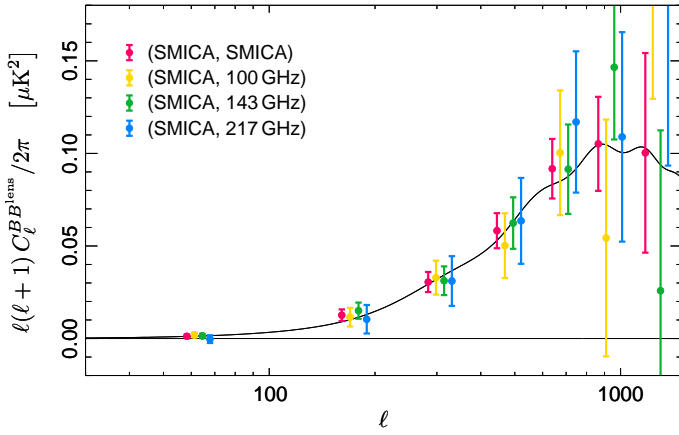


Figure 8. Stability to the change in the observed polarization map. Data points show the $C_\ell^{BB\text{lens}}$ band-powers obtained from the cross-correlation of our SMICA B -mode template with the SMICA polarization map (red), as well as to single frequency polarization maps at 100 GHz (yellow), 143 GHz (green), and 217 GHz (blue), which were corrected for foreground and intensity-to-polarization leakage.

is negligible, such a *direct* method can be used to measure the lensing C_ℓ^{BB} , as reported by the POLARBEAR (The Polarbear Collaboration: P. A. R. Ade et al. 2014) and SPTpol (Keisler et al. 2015) teams. In order to probe the secondary contribution only, the B -mode power spectrum can also be measured using an *indirect* method, relying on cross-correlation with a lensing B -mode template, as reported in Hanson et al. (2013), Ade et al. (2014b), Planck Collaboration XV (2016), and in the present paper. These composite measurements are gathered in Fig. 9, showing the landscape of current CMB BB band-power estimates.

The BICEP2/Keck Array BB band-powers that are shown in Fig. 9 correspond to the B -mode determinations in the multipole range $20 < \ell < 335$, obtained from the combination of the BICEP2 and Keck Array maps, as reported in BICEP2 and Keck Array Collaborations et al. (2015a) and corrected for polarized dust emission using *Planck* data, as described in BICEP2/Keck Array and Planck Collaborations (2015) (which is referred to as BKP hereafter). The POLARBEAR C_ℓ^{BB} *direct* measurement in the multipole range $500 < \ell < 2100$ reported in The Polarbear Collaboration: P. A. R. Ade et al. (2014), are also plotted. For the *indirect* cross-correlations lensing B -mode measurements, Fig. 9 shows the SPTpol and *Planck* C_ℓ^{BB} band-powers. The SPTpol band-powers correspond to measurements in the multipole range $300 < \ell < 2750$ reported in Hanson et al. (2013), which used a B -mode template synthesized from the SPTpol E -mode map and the *Herschel*-SPIRE cosmic infrared background map. For our fiducial $C_\ell^{BB\text{lens}}$ band-powers, we select the conservative $f_{\text{sky}} = 0.7$ analysis, which are consistent with both the most conservative $f_{\text{sky}} = 0.6$ band-powers and the most optimistic $f_{\text{sky}} = 0.8$ band-powers, as discussed in Sect. 6.1. Note that the POLARBEAR team also reported a 4.2σ lensing BB measurement, based on the cross-correlation method in (Ade et al. 2014b), which is not shown in the figure.

Our *Planck*-derived $C_\ell^{BB\text{lens}}$ band-powers are in good agreement with other measurements, using both the *indirect* or *direct* methods. We recall the fact that *Planck* provides the best

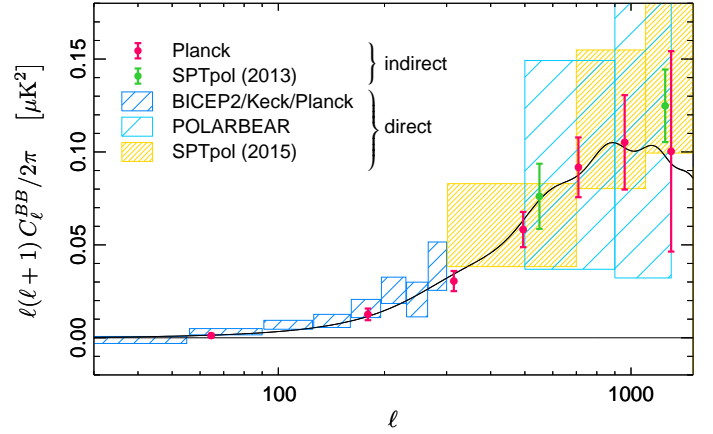


Figure 9. Consistency with external CMB lensing B -mode power spectrum measurements. We compare our fiducial estimate (red points) to the SPTpol cross-correlation results (green points) (Hanson et al. 2013), as well as to the *direct* auto- C_ℓ^{BB} measurements from BICEP2/Keck Array (blue boxes) (BICEP2 and Keck Array Collaborations et al. 2015a), POLARBEAR (light blue boxes) (The Polarbear Collaboration: P. A. R. Ade et al. 2014), and SPTpol (yellow boxes) (Keisler et al. 2015), as discussed in Sect. 6.3. The black line shows the theoretical lensing B -mode power spectrum for the base Λ CDM best-fit *Planck* model (with $r = 0$).

measurement of the lensing-induced B -mode power spectrum to date (as assessed in Planck Collaboration XV 2016). Covering a wide multipole range $10 < \ell < 2000$, our band-powers consists of lensing C_ℓ^{BB} measurements at a significance level as high as 12σ . It is also worth focusing on the low- ℓ part of Fig. 9, which gives an indication of the lensing B -mode template utility for the primordial-to-secondary B -modes discrimination. Using *Planck* data alone, which combines wide sky coverage, necessary to probe low multipoles, and a good angular resolution, needed for the lensing potential extraction, our lensing B -mode template enables us to extend the measure of the lensing-induced C_ℓ^{BB} into the low multipole range.

7. Implications for current and future B -mode experiments

In the previous sections, the characteristics of the *Planck* lensing B -mode template have been described and its robustness discussed. Here, we will address the implications of the template for experiments targeting primordial B -modes. A full joint analysis using external data is beyond the scope of this paper. However, as examples we discuss two different aspects. First, we address to what extent the template can help experiments in measuring the lensing B -mode power spectrum, in particular over the largest accessible angular scales. As in Sect. 6.3, we consider the BICEP2/Keck Array combination, POLARBEAR, and SPTpol. Secondly, we forecast the improvement of the lensing amplitude measurement when using the *Planck* lensing B -mode template, and we discuss whether this improvement can translate into a better sensitivity to the tensor-to-scalar ratio. Following the joint analysis in BKP, we consider first the BICEP2/Keck Array combination. We also derive forecasts for future wide sky coverage projects, such as LiteBIRD (Matsumura et al. 2014).

7.1. Measurement of the lensing B -mode power spectrum

Since the *Planck* lensing B -mode template covers almost the entire sky, any B -mode experiment can be cross-correlated with the template in its covered sky area. This ensures a valuable lensing B -mode power spectrum (indirect) measurement, including the intermediate angular scales, where the lensing signal is of the same order of magnitude or sub-dominant with respect to the polarized foreground emission (see [Planck Collaboration Int. XXX 2014](#), hereafter referred to as PIP-XXX).

For current ground-based experiments, the cross-correlation with the *Planck* template is a promising method for measuring the lensing B -mode signal at the largest accessible angular scales. In general, it leads to better results than a cross-correlation with a lensing B -mode template built out of the *Planck* lensing potential and each experiment's E -mode map. This can be understood from two different considerations. On the one hand, a study of the lensing B -mode signal kernel (as in [Fabbian & Stompor 2013](#)) reveals that most of the signal at low and intermediate angular scales comes from products of the lensing potential power at low multipoles and the E -mode power at higher multipoles. For example, at $\ell = 100$ (200), 80 % (90 %) of the lensing B -mode power arises from E -mode power at $\ell > 335$. For degree-scale experiments, such as BICEP, it would be of little value to use its own E -mode data in order to generate a new lensing B -mode template. On the other hand, we studied the lensing B -mode power spectrum uncertainties that originate from the template itself, by ranking the various contributions that enter the template auto-power spectrum. We found that the noise power spectrum of the reconstructed lensing potential N_L^ϕ (see [Planck Collaboration XV 2016](#)) induces the dominant contribution, whereas the E -mode noise power spectrum contributes a maximum of 35 % of the total power over the range $10 < \ell < 500$. For experiments covering less than a percent of the sky, such as SPTpol or POLARBEAR, the improvement of the lensing B -mode power spectrum uncertainties arising from the lower E -mode noise would be of the same order as that lost due to the low- ℓ cut, giving at best no net uncertainty gain.

7.1.1. Uncertainty forecasting method

We forecast the uncertainties of the lensing B -mode power spectrum indirect measurement that current experiments can obtain from cross-correlating their B -mode signal with the *Planck* lensing B -mode template. As in Sect. 6.3, we consider the BICEP2/Keck Array, POLARBEAR, and SPTpol examples. Error bars are evaluated using Eq. (14). They include lensed cosmic variance from the best-fit Λ CDM model and the statistical error from the template (the template auto-power spectrum $\hat{C}_\ell^{B\text{lens}}$ factor) and from the experiment (the experiment auto-spectrum $(C_\ell^B + N_\ell^B)$ factor). In order to estimate the template variance within the experiment's field, $\hat{C}_\ell^{B\text{lens}}$ is analytically calculated using the lensing potential and E -mode noise power spectra, rescaled to the noise spatial inhomogeneity within the experiment's field. This rescaling relies on the SMICA hit count map. We use a simplified model for the BB auto-spectrum of the experiment that includes the lensed CMB B -modes, polarized dust, white noise, and Gaussian beam.

The polarized dust emission is parametrized by a single free amplitude in power, A_{dust} , which is defined at the reference frequency of 353 GHz and at a multipole of $\ell = 80$. Following PIP-XXX, the dust power spectrum is modelled as the power law $C_\ell^{\text{dust}} \propto \ell^{-2.42}$, with a spatially uniform frequency scaling

according to a modified blackbody law, assuming a fixed dust temperature $T_d = 19.6$ K and spectral index $\beta_d = 1.6$. For the BICEP2/Keck Array combination, we fix the dust amplitude to the best-fit value obtained in the joint BICEP2/Keck Array and *Planck* analysis described in BKP, namely $A_{\text{dust}} = 3 \mu\text{K}^2$. In PIP-XXX, individual dust amplitudes have been fitted for a series of sky patches, and their scaling with the mean 353 GHz dust intensity was described using an empirical relation. However, there was a warning about the difficulty in deriving precise dust amplitude estimates from this empirical law. From figure 7 of PIP-XXX, we can see that, at the low dust intensity values expected in the SPTpol and POLARBEAR fields, the amplitudes range from 0.1 to $10 \mu\text{K}^2$. For simplicity, we assume the level of dust emission in the POLARBEAR and SPTpol fields to be the same as in the BICEP2 field, and so use the value $A_{\text{dust}} = 3 \mu\text{K}^2$. We checked that assuming the more pessimistic $A_{\text{dust}} = 10 \mu\text{K}^2$ leads to a minor increase of the forecasted B -lensing band-power uncertainties.

The BICEP2/Keck Array combination is modelled as reaching a noise level of $3.4 \mu\text{K} \cdot \text{arcmin}$ over 400 deg^2 , and as having a Gaussian beam of $31'$ FWHM for both BICEP2 and Keck Array experiments ([BICEP2 and Keck Array Collaborations et al. 2015b,a](#)). POLARBEAR is modelled as reaching a depth of $8 \mu\text{K} \cdot \text{arcmin}$ over an effective sky area of 25 deg^2 ($f_{\text{sky}} = 0.06 \%$) with $3.5'$ resolution at 150 GHz ([The Polarbear Collaboration: P. A. R. Ade et al. 2014](#)). For SPTpol, we model the noise spectrum from the characteristics reported in [Hanson et al. \(2013\)](#), by considering the combination of the 95 GHz observation ($1.83'$ resolution and $25 \mu\text{K} \cdot \text{arcmin}$ noise level) and the 150 GHz observation ($1.06'$ resolution and $10 \mu\text{K} \cdot \text{arcmin}$ noise level) over a sky area of 100 deg^2 ($f_{\text{sky}} = 0.24 \%$). We use the same multipole binning as chosen by each experiment in existing publications, and consider an additional low- ℓ bin including multipoles up to the largest accessible angular scales defined by the experiment's sky coverage. For POLARBEAR and SPTpol, we consider the $100 < \ell < 2000$ multipole range.

7.1.2. Lensing B -mode band-power forecasts

Figure 10 shows the forecasted lensing B -mode band-powers over multipoles up to 500, for which the *Planck* lensing B -mode template is the most useful in helping other experiments to determine the lensing B -mode power spectrum. We find that the BICEP2/Keck Array could be used in combination with the *Planck* lensing B -mode template to obtain a measurement of the lensing B -mode band-powers in the multipole range $\ell = 20$ –335 at a significance level of about 6σ (sensitivity to $A_{B\text{lens}}$ of 0.17). This indicates that the *Planck* template enables sub-degree angular scale experiments, such as BICEP2/Keck Array, to probe the ℓ -dependence of the lensing B -mode signal over their full multipole range, including multipoles at which the lensing-induced signal is sub-dominant compared to other sources of B -mode signal (such as polarized dust). Note also that this result relies on the $\hat{C}_\ell^{BB\text{lens}}$ cross-spectrum information only. Accounting for additional information within the BB auto-power spectra of the experiment and the template further improves the precision to which the lensing B -mode signal can be detected (as we shall see in Sect. 7.3). Moreover, the cross-correlation with the template should allow experiments targeting higher multipoles (such as POLARBEAR or SPTpol) to measure the lensing B -mode signal at intermediate angular scales ($100 < \ell < 300$), extending their own direct or indirect estimates down to as low multipoles as their sky coverage and systematic effects would permit.

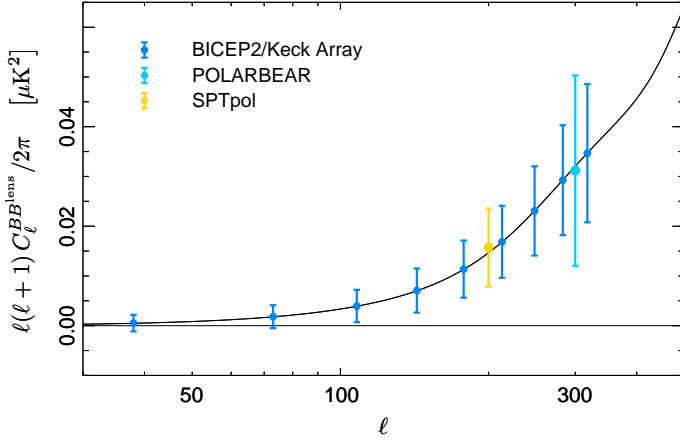


Figure 10. Forecasts of lensing B -mode band-powers from cross-correlating the *Planck* lensing B -mode template with external data from B -mode targeted experiments. Blue circles show the BICEP2/Keck Array band-powers forecasts using the same multipole binning as that of BICEP2/Keck Array data points shown in Fig. 9. Indirect lensing B -mode band-power measurements can be extended to an additional $\ell = 100$ –500 bin using POLARBEAR (lighter shade of blue) and to an additional $\ell = 100$ –300 bin using the SPTpol (yellow) in cross-correlation with the template.

7.2. Direct delensing capabilities

“Delensing” consists of subtracting the lensing B -mode template from the B -mode map of an experiment in order to try to highlight the primordial B -modes. Due to the noise level of the template, poor efficiency is expected from a direct delensing approach (e.g., [Marian & Bernstein 2007](#)). In order to quantify the expected impact on the tensor-to-scalar ratio uncertainty, we calculate the improvement factor as defined in [Smith et al. \(2009b\)](#) as

$$\alpha = \frac{C_\ell^{B,\text{lens}} + N_\ell^B}{C_\ell^{B,\text{res}} + N_\ell^B}. \quad (15)$$

Here $C_\ell^{B,\text{lens}}$ and $C_\ell^{B,\text{res}}$ are the lensing B -mode power spectrum, and its residual after subtraction of the template from the external data, while N_ℓ^B is the noise power spectrum of the experiment. We find a maximum improvement factor (corresponding to $N_\ell^B = 0$) of 5 % at $\ell < 200$, reaching a maximum of 10 % around $\ell = 300$, in agreement with the expectations derived in [Smith et al. \(2009b\)](#).

7.3. Improvement of the parameter accuracies

We now go beyond the lensing B -mode power spectrum measurement and quantify whether the use of the template as an additional data set (together with other B -mode data and the *Planck* dust template) can tighten cosmological parameter constraints, and in particular, the amplitude of the lensing potential power spectrum that scales the lensing-induced B -modes, A_{lens} . We discuss whether better measurements of the lensing scaling translate into tightened constraints on the tensor-to-scalar ratio.

In order to derive forecasts for particular experiments, we will perform a Fisher analysis⁸ (for a description of this method,

see e.g., [Tegmark et al. 1997](#)). We consider a three-parameter model, $\{r, A_{\text{lens}}, A_{\text{dust}}\}$, consisting of the tensor-to-scalar ratio and the amplitudes of the lensing potential and polarized dust power spectra. We will compare the parameter constraints obtained in two cases: (1) the data sets consist of B^{exp} , the external data from the B -mode targeted experiment, and \hat{B}^{dust} , the *Planck* B -mode data at 353 GHz, considered as a polarized dust template; and (2) the *Planck* lensing B -mode template, \hat{B}^{lens} , is used in combination with the other two data sets. As examples of external experiments, we consider first the BICEP2/Keck Array combination, hereafter referred to as BK, described in [BICEP2 and Keck Array Collaborations et al. \(2015a\)](#), as well as a wide sky coverage experiment, such as LiteBIRD ([Matsumura et al. 2014](#)). The rationale driving these choices is twofold. Due to the lensing B -mode template noise level in a 1 % sky area and from the results obtained above, we do not expect the inclusion of the template to bring a large improvement of the sensitivity to r for BK. However, we will be able to validate our simple fiducial analysis by comparing to the analysis described in BKP (our case 1), corresponding to the extension with a floating lensing amplitude considered in BKP. By contrast, a more substantial improvement is expected for a large sky coverage B -mode experiment such as LiteBIRD. For definiteness, we will consider the sensitivity to an $r = 0.05$ fiducial model in what follows.

7.3.1. Fisher analysis

We consider the Fisher information matrix of the form (see e.g., [Tegmark et al. 1997](#))

$$F_{ij} = \sum_\ell \frac{1}{2} (2\ell + 1) f_{\text{sky}} \text{Tr}[\mathbf{C}\mathbf{C}_{,i}\mathbf{C}\mathbf{C}_{,j}] \quad (16)$$

for a fiducial data covariance matrix \mathbf{C} and its derivatives with respect to the parameters labelled by i and j . Given the data set $\{B_{\ell m}^{\text{exp}}, \hat{B}_{\ell m}^{\text{dust}}, \hat{B}_{\ell m}^{\text{lens}}\}$, we need to model the B -mode auto-power spectra for the external data, C_ℓ^{exp} , for the *Planck* 353 GHz map, C_ℓ^{353} , and for the *Planck* lensing B -mode template within the experiment’s sky coverage, $C_\ell^{\hat{B}^{\text{lens}}}$, as well as the corresponding cross-power spectra.

The fiducial model consists of an extension of the 6-parameter Λ CDM model considered so far, including primordial gravitational waves (GW) of amplitude r , a free amplitude of the lensing potential power spectrum, A_{lens} , and a free polarized dust amplitude in power A_{dust} (defined at the reference frequency of 353 GHz and at a multipole of $\ell = 80$). In this fiducial framework, the B -mode auto-power spectrum of the experiment under consideration is

$$C_\ell^{\text{exp}} = \frac{r}{0.05} C_\ell^{\text{GW}, r=0.05} + A_{\text{lens}} C_\ell^{\text{lens}} + \alpha A_{\text{dust}} R(\nu, 353)^2 C_\ell^{\text{dust}} + N_\ell^{\text{exp}}, \quad (17)$$

where C_ℓ^{GW} and C_ℓ^{lens} are the gravitational wave and lensing power spectra at the fiducial $r = 0.05$ and $A_{\text{lens}} = 1$ values. The dust power spectrum, C_ℓ^{dust} , and its frequency scaling with the reference 353 GHz frequency, $R(\nu, 353)$ are modelled as in Sect. 7.1, following PIP-XXX. In addition, for multi-band experiments with foreground-cleaning capabilities, the dust power spectrum is assumed to be cleaned up to a residual level defined by the α factor ($\alpha = 1$ for a single frequency experiment).

be derived by calculating the distribution Hessian taken at the fiducial values of the parameters. Due to this assumption, parameter confidence contours are ellipses.

⁸Note that in this approach, the parameter likelihood is assumed to be Gaussian close to its maximum, so that the parameter constraints can

Finally, N_ℓ^{exp} is the B -mode noise power spectrum of each experiment.

The *Planck* 353 GHz B -mode auto-power spectrum in each experiment's sky coverage is modelled as

$$C_\ell^{353} = A_{\text{dust}} C_\ell^{\text{dust}} + N_\ell^{353}, \quad (18)$$

where the full-sky noise power spectrum at 353 GHz is scaled to account for the spatial inhomogeneity within the experimental field. We neglect the sub-dominant CMB B -mode polarization signal.

Finally, the *Planck* lensing B -mode template auto-power spectrum within the experimental field is analytically calculated using

$$C_\ell^{\text{B lens}} = \mathcal{B}_\ell^{-2} \sum_{L, L'} (f_L^\phi)^2 (C_L^{\phi, \text{fid}} + N_L^\phi) (f_{L'}^E)^2 (C_{L'}^{E, \text{fid}} + N_{L'}^E) {}_2F_{LL'}, \quad (19)$$

where the noise power spectra of the lensing potential N_L^ϕ and of the E -mode $N_{L'}^E$ are scaled to account for the spatial inhomogeneity within the experimental field. The cross-correlation of the experiment's data with the 353 GHz dust template and lensing B -mode template are $(\alpha)^{0.5} A_{\text{dust}} R(\nu, 353) C_\ell^{\text{dust}}$ and C_ℓ^{lens} . Following the assumptions of the model, we neglect the sub-dominant cross-correlation of the lensing B -mode and 353 GHz dust templates.

7.3.2. Examples of BK and LiteBIRD

For existing data, we use a data-driven model. Both the BK and the *Planck* 353 GHz noise power spectra in the BK field are extrapolated from the noise band-powers released along with the BKP likelihood.⁹ For the future project LiteBIRD, we model the noise power spectrum from the foreseen instrumental characteristics defined in Matsumura et al. (2014). Only the 100 and 140 GHz bands are considered, the two lowest and two highest bands being discarded, assuming that they will be used for foreground cleaning. Following Matsumura et al. (2014), the 100 GHz band reaches a depth of $3.7 \mu\text{K.arcmin}$ and a resolution defined by a Gaussian beam of $45'$ FWHM, while the 140 GHz band has a noise level of $4.7 \mu\text{K.arcmin}$ and $32'$ FWHM. The polarized dust in each frequency band is assumed to be cleaned over an effective sky area of 63 % up to the same residual level as in the BK field. This corresponds to a mildly conservative (Dunkley et al. 2009) 17 % residual level in the map domain (corresponding to $\alpha = 2.9$ % in power) for the dust amplitude $A_{\text{dust}} = 104.5 \mu\text{K}^2$, obtained in PIP-XXX via a power-law fit in the large retained science region "LR63."

With the fiducial model established and using the numerical analysis method described, we can infer the sensitivity to the parameters as $\Delta\theta_i = \sqrt{(F^{-1})_{ii}}$ for $\theta_i \in \{r, A_{\text{lens}}, A_{\text{dust}}\}$. The results for BK and LiteBIRD in the two cases considered, depending on whether the lensing B -mode template is used or not, are presented in Table 2.

For the BK analysis in Case 1 (without the lensing template), we find $\Delta r = 0.031$, $\Delta A_{\text{lens}} = 0.186$ and $\Delta A_{\text{dust}} = 0.7$, in agreement with results reported in BKP: $r = 0.048^{+0.035}_{-0.032}$, $A_{\text{lens}} = 1.13 \pm 0.18$ (from the free lensing amplitude extended analysis) and $A_{\text{dust}} = 3.3^{+0.9}_{-0.8}$. This indicates that our fiducial Fisher analysis yields reliable parameter uncertainty estimates despite the underlying simplifying assumptions. The use of the lensing template translates into a 5 % improvement of the r constraint, whereas the constraint on A_{lens} is tightened by 36 %. Over

Table 2. Fisher analysis inferred parameter uncertainties for the BICEP2/Keck Array experiment and for the LiteBIRD project. Forecasts are given for two different data sets: case 1 consists of the experiment's data and the *Planck* 353 GHz map; and case 2 consists of the same two ingredients plus the *Planck* lensing B -mode template.

Parameter	BICEP2/Keck ^a		LiteBIRD ^b	
	Case 1	Case 2	Case 1	Case 2
Δr	0.031	0.030	0.0021	0.0018
ΔA_{lens} . . .	0.19	0.12	0.042	0.033
ΔA_{dust} . . .	0.7	0.6	0.05	0.05

^a See BICEP2 and Keck Array Collaborations et al. (2015a).

^b See Matsumura et al. (2014).

the multipole range covered by BK, A_{lens} is weakly correlated with both r and A_{dust} , as was noted in the BKP paper, so that the improvement in the A_{lens} constraint translates into modest improvement of the r or A_{dust} constraints. This is verified in Fig. 11, where the 2-dimensionnal contours at 68 % and 95 % are shown in the $A_{\text{lens}}-r$ and $A_{\text{lens}}-A_{\text{dust}}$ planes. However, Fig. 11 also shows that the $A_{\text{lens}}-r$ correlation is further reduced when the lensing B -mode template is used, leading to more robust constraints.

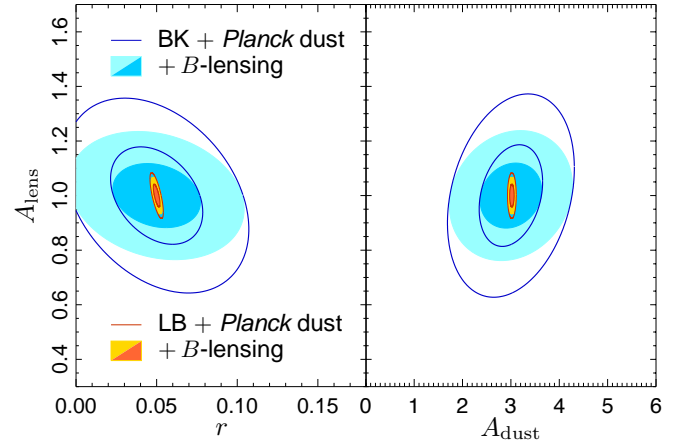


Figure 11. Constraints on the tensor-to-scalar ratio r and the amplitude of the polarized dust power A_{dust} within a model with free lensing potential amplitude A_{lens} . The 2-dimensionnal likelihood contours at 68 % and 95 % are forecast for BICEP2/Keck Array (BK, shades of blue) and for LiteBIRD (LB, shades of red), in combination with the *Planck* 353 GHz dust template only (line contours) and the *Planck* dust and lensing B -mode templates (shaded contours).

For large angular scale experiments whose multipole coverage is limited to $\ell \lesssim 200$, such as LiteBIRD, the improvement is larger. The lack of measurement over a lensing B -mode dominated multipole range increases the parameter degeneracy, in particular between A_{lens} and r , as seen in Fig. 11. The 20 % improvement on the A_{lens} uncertainties, which arises from using the *Planck* lensing B -mode template, translates into a 15 % improvement on the r uncertainties.

⁹http://bicepkeck.org/bkp2_2015_release.html

8. Conclusions

We have produced a nearly all-sky template of the CMB secondary B -modes using the *Planck* full-mission foreground-cleaned CMB temperature and Stokes parameter maps. For this purpose, we have developed a dedicated pipeline that has been verified via specific simulations. We show that the constructed template includes the lensing B -mode contribution at all angular scales covered by *Planck* and shows no contamination from primordial B -modes. This template has been used to compute the CMB lensing B -mode power spectrum by cross-correlating it with the total foreground-cleaned *Planck* polarization B -mode maps (via the publicly available Q and U maps). We find that the resulting CMB lensing B -mode power spectrum is insensitive to foreground contamination and independent of the choice of the foreground-cleaned *Planck* polarization B -mode map used for the cross-correlation analysis. Furthermore, we find that the results are in good agreement with the expected CMB lensing B -mode power spectrum computed using the baseline *Planck* 2015 best-fitting Λ -CDM model. We obtain a 12σ detection of the lensing B -modes, in agreement with the results in the companion [Planck Collaboration XV \(2016\)](#) paper.

Planck provides a unique nearly all-sky lensing B -mode template, containing all the lens-induced information from intermediate to large angular scales. This template, which is included as part of the *Planck* 2015 data release, will be a useful tool for current and future ground-based experiments targeting the measurement of the primordial CMB B -mode power spectrum. Indeed, this template can be used to obtain a reliable (indirect) measurement of the lensing B -mode power spectrum with future experiments or to improve the precision with which they can (directly) detect the lensing B -modes in their own data, by tightening the constraints on the lensing amplitude. This, in turn, can help in the much more challenging endeavour of constraining the tensor-to-scalar ratio.

Acknowledgements. The Planck Collaboration acknowledges the support of: ESA; CNES, and CNRS/INSU-IN2P3-INP (France); ASI, CNR, and INAF (Italy); NASA and DoE (USA); STFC and UKSA (UK); CSIC, MINECO, JA and RES (Spain); Tekes, AoF, and CSC (Finland); DLR and MPG (Germany); CSA (Canada); DTU Space (Denmark); SER/SSO (Switzerland); RCN (Norway); SFI (Ireland); FCT/MCTES (Portugal); ERC and PRACE (EU). A description of the Planck Collaboration and a list of its members, indicating which technical or scientific activities they have been involved in, can be found at <http://www.cosmos.esa.int/web/planck>. This paper made use of the HEALPix software package.

References

Abrial, P., Moudden, Y., Starck, J., et al., Morphological Component Analysis and Inpainting on the sphere: Application in Physics and Astrophysics. 2007, J. Fourier Anal. and Applic., 13, 729

Ade, P. A. R., Aikin, R. W., Barkats, D., et al., Detection of B-Mode Polarization at Degree Angular Scales by BICEP2. 2014a, Phys. Rev. Lett., 112, 241101, [arXiv:1403.3985](#)

Ade, P. A. R., Akiba, Y., Anthony, A. E., et al., Measurement of the Cosmic Microwave Background Polarization Lensing Power Spectrum with the POLARBEAR Experiment. 2014b, Phys. Rev. Lett., 113, 021301

Benoit-Lévy, A., Déchelette, T., Benabed, K., et al., Full-sky CMB lensing reconstruction in presence of sky-cuts. 2013, A&A, 555, A37, [arXiv:1301.4145](#)

BICEP2 and Keck Array Collaborations, Ade, P. A. R., Ahmed, Z., et al., BICEP2/Keck Array V: Measurements of B-mode Polarization at Degree Angular Scales and 150 GHz by the Keck Array. 2015a, ApJ, 811, 126, [arXiv:1502.00643](#)

BICEP2 and Keck Array Collaborations, Ade, P. A. R., Aikin, R. W., et al., BICEP2/Keck Array. IV. Optical Characterization and Performance of the BICEP2 and Keck Array Experiments. 2015b, ApJ, 806, 206, [arXiv:1502.00596](#)

BICEP2/Keck Array and Planck Collaborations, Joint Analysis of BICEP2/Keck Array and Planck Data. 2015, Phys. Rev. Lett., 114, 101301, [arXiv:1502.00612](#)

Delabrouille, J., Cardoso, J.-F., & Patanchon, G., Multidetector multicomponent spectral matching and applications for cosmic microwave background data analysis. 2003, MNRAS, 346, 1089, [arXiv:astro-ph/0211504](#)

Dunkley, J., Amblard, A., Baccigalupi, C., et al. 2009, in American Institute of Physics Conference Series, Vol. 1141, American Institute of Physics Conference Series, ed. S. Dodelson, D. Baumann, A. Cooray, J. Dunkley, A. Fraisse, M. G. Jackson, A. Kogut, L. Krauss, M. Zaldarriaga, & K. Smith, 222–264

Fabbian, G. & Stompor, R., High-precision simulations of the weak lensing effect on cosmic microwave background polarization. 2013, A&A, 556, A109, [arXiv:1303.6550](#)

Górski, K. M., Hivon, E., Banday, A. J., et al., HEALPix: A Framework for High-Resolution Discretization and Fast Analysis of Data Distributed on the Sphere. 2005, ApJ, 622, 759, [arXiv:astro-ph/0409513](#)

Grishchuk, L. P., Amplification of gravitational waves in an isotropic universe. 1975, Sov. J. Exp. Theor. Phys., 40, 409

Guth, A. H., Inflationary universe: A possible solution to the horizon and flatness problems. 1981, Phys. Rev. D, 23, 347

Hanson, D., Hoover, S., Crites, A., et al., Detection of B-Mode Polarization in the Cosmic Microwave Background with Data from the South Pole Telescope. 2013, Phys. Rev. Lett., 111, 141301, [arXiv:1307.5830](#)

Hu, W., Weak lensing of the CMB: A harmonic approach. 2000, Phys. Rev. D, 62, 043007, [arXiv:astro-ph/0001303](#)

Kamionkowski, M., Kosowsky, A., & Stebbins, A., A Probe of Primordial Gravity Waves and Vorticity. 1997, Phys. Rev. Lett., 78, 2058, [arXiv:astro-ph/9609132](#)

Keisler, R., Hoover, S., Harrington, N., et al., Measurements of Sub-degree B-mode Polarization in the Cosmic Microwave Background from 100 Square Degrees of SPTpol Data. 2015, ApJ, 807, 151, [arXiv:1503.02315](#)

Knox, L., Determination of inflationary observables by cosmic microwave background anisotropy experiments. 1995, Phys. Rev. D, 52, 4307, [arXiv:astro-ph/9504054](#)

Lewis, A. & Challinor, A., Weak gravitational lensing of the CMB. 2006, Phys. Rep., 429, 1, [arXiv:astro-ph/0601594](#)

Linde, A. D., A new inflationary universe scenario: A possible solution of the horizon, flatness, homogeneity, isotropy and primordial monopole problems. 1982, Phys. Lett. B, 108, 389

Marian, L. & Bernstein, G. M., Detectability of CMB tensor B modes via de-lensing with weak lensing galaxy surveys. 2007, Phys. Rev. D, 76, 123009, [arXiv:0710.2538](#)

Matsumura, T., Akiba, Y., Borrill, J., et al., Mission Design of LiteBIRD. 2014, J. Low Temp. Phys., 176, 733, [arXiv:1311.2847](#)

Okamoto, T. & Hu, W., Cosmic microwave background lensing reconstruction on the full sky. 2003, Phys. Rev. D, 67, 083002, [arXiv:astro-ph/0301031](#)

Perotto, L., Bobin, J., Plaszczynski, S., Starck, J.-L., & Lavabre, A., Reconstruction of the cosmic microwave background lensing for Planck. 2010, A&A, 519, A4

Planck Collaboration XVIII, *Planck* early results. XVIII. The power spectrum of cosmic infrared background anisotropies. 2011, A&A, 536, A18, [arXiv:1101.2028](#)

Planck Collaboration XII, *Planck* 2013 results. XII. Diffuse component separation. 2014, A&A, 571, A12, [arXiv:1303.5072](#)

Planck Collaboration XIII, *Planck* 2013 results. XIII. Galactic CO emission. 2014, A&A, 571, A13, [arXiv:1303.5073](#)

Planck Collaboration XVI, *Planck* 2013 results. XVI. Cosmological parameters. 2014, A&A, 571, A16, [arXiv:1303.5076](#)

Planck Collaboration XVIII, *Planck* 2013 results. XVIII. The gravitational lensing-infrared background correlation. 2014, A&A, 571, A18, [arXiv:1303.5078](#)

Planck Collaboration XXVIII, *Planck* 2013 results. XXVIII. The Planck Catalogue of Compact Sources. 2014, A&A, 571, A28, [arXiv:1303.5088](#)

Planck Collaboration XXIX, *Planck* 2013 results. XXIX. The Planck catalogue of Sunyaev-Zeldovich sources. 2014, A&A, 571, A29, [arXiv:1303.5089](#)

Planck Collaboration I, *Planck* 2015 results. I. Overview of products and results. 2016, A&A, submitted, [arXiv:1502.01582](#)

Planck Collaboration II, *Planck* 2015 results. II. Low Frequency Instrument data processing. 2016, A&A, submitted, [arXiv:1502.01583](#)

Planck Collaboration III, *Planck* 2015 results. III. LFI systematic uncertainties. 2016, A&A, submitted, [arXiv:1507.08853](#)

Planck Collaboration IV, *Planck* 2015 results. IV. LFI beams and window functions. 2016, A&A, in press, [arXiv:1502.01584](#)

Planck Collaboration V, *Planck* 2015 results. V. LFI calibration. 2016, A&A, in press, [arXiv:1505.08022](#)

Planck Collaboration VI, *Planck* 2015 results. VI. LFI maps. 2016, A&A, submitted, [arXiv:1502.01585](#)

Planck Collaboration VII, *Planck* 2015 results. VII. High Frequency Instrument data processing: Time-ordered information and beam processing. 2016, A&A, in press, [arXiv:1502.01586](#)

- Planck Collaboration VIII, *Planck* 2015 results. VIII. High Frequency Instrument data processing: Calibration and maps. 2016, A&A, in press, [arXiv:1502.01587](#)
- Planck Collaboration IX, *Planck* 2015 results. IX. Diffuse component separation: CMB maps. 2016, A&A, submitted, [arXiv:1502.05956](#)
- Planck Collaboration X, *Planck* 2015 results. X. Diffuse component separation: Foreground maps. 2016, A&A, submitted, [arXiv:1502.01588](#)
- Planck Collaboration XII, *Planck* 2015 results. XII. Full Focal Plane simulations. 2016, A&A, submitted, [arXiv:1509.06348](#)
- Planck Collaboration XIII, *Planck* 2015 results. XIII. Cosmological parameters. 2016, A&A, submitted, [arXiv:1502.01589](#)
- Planck Collaboration XV, *Planck* 2015 results. XV. Gravitational lensing. 2016, A&A, submitted, [arXiv:1502.01591](#)
- Planck Collaboration XX, *Planck* 2015 results. XX. Constraints on inflation. 2016, A&A, submitted, [arXiv:1502.02114](#)
- Planck Collaboration XXII, *Planck* 2015 results. XXII. A map of the thermal Sunyaev-Zeldovich effect. 2016, A&A, submitted, [arXiv:1502.01596](#)
- Planck Collaboration XXVI, *Planck* 2015 results. XXVI. The Second Planck Catalogue of Compact Sources. 2016, A&A, submitted, [arXiv:1507.02058](#)
- Planck Collaboration XXVII, *Planck* 2015 results. XXVII. The Second Planck Catalogue of Sunyaev-Zeldovich Sources. 2016, A&A, in press, [arXiv:1502.01598](#)
- Planck Collaboration Int. XXX, *Planck* intermediate results. XXX. The angular power spectrum of polarized dust emission at intermediate and high Galactic latitudes. 2014, A&A, in press, [arXiv:1409.5738](#)
- Plaszczynski, S., Lavabre, A., Perotto, L., & Starck, J.-L., A hybrid approach to cosmic microwave background lensing reconstruction from all-sky intensity maps. 2012, A&A, 544, A27, [arXiv:1201.5779](#)
- Polnarev, A. G., Polarization and Anisotropy Induced in the Microwave Background by Cosmological Gravitational Waves. 1985, Soviet Ast., 29, 607
- Seljak, U. & Zaldarriaga, M., Signature of Gravity Waves in the Polarization of the Microwave Background. 1997, Phys. Rev. Lett., 78, 2054, [arXiv:astro-ph/9609169](#)
- Sherwin, B. D. & Schmittfull, M., Delensing the CMB with the cosmic infrared background. 2015, Phys. Rev. D, 92, 043005, [arXiv:1502.05356](#)
- Smith, K. M., Cooray, A., Das, S., et al. 2009a, in American Institute of Physics Conference Series, Vol. 1141, American Institute of Physics Conference Series, ed. S. Dodelson, D. Baumann, A. Cooray, J. Dunkley, A. Fraisse, M. G. Jackson, A. Kogut, L. Krauss, M. Zaldarriaga, & K. Smith, 121–178
- Smith, K. M., Cooray, A., Das, S., et al. 2009b, in American Institute of Physics Conference Series, Vol. 1141, American Institute of Physics Conference Series, ed. S. Dodelson, D. Baumann, A. Cooray, J. Dunkley, A. Fraisse, M. G. Jackson, A. Kogut, L. Krauss, M. Zaldarriaga, & K. Smith, 121–178
- Song, Y.-S., Cooray, A., Knox, L., & Zaldarriaga, M., The Far-Infrared Background Correlation with Cosmic Microwave Background Lensing. 2003, ApJ, 590, 664, [arXiv:astro-ph/0209001](#)
- Spergel, D. N. & Zaldarriaga, M., Cosmic Microwave Background Polarization as a Direct Test of Inflation. 1997, Phys. Rev. Lett., 79, 2180, [arXiv:astro-ph/9705182](#)
- Starobinsky, A. A., Spectrum of gravitational background radiation and initial state of the universe. 1979, Pisma v Zh. Eksp. Teor. Fiz., 30, 719
- Starobinsky, A. A., Dynamics of phase transition in the new inflationary universe scenario and generation of perturbations. 1982, Phys. Lett. B, 117, 175
- Tegmark, M., Taylor, A. N., & Heavens, A. F., Karhunen-Loève Eigenvalue Problems in Cosmology: How Should We Tackle Large Data Sets? 1997, ApJ, 480, 22, [arXiv:astro-ph/9603021](#)
- The Polarbear Collaboration: P. A. R. Ade, Akiba, Y., Anthony, A. E., et al., A Measurement of the Cosmic Microwave Background B-mode Polarization Power Spectrum at Sub-degree Scales with POLARBEAR. 2014, ApJ, 794, 171, [arXiv:1403.2369](#)
- van Engelen, A., Sherwin, B. D., Sehgal, N., et al., The Atacama Cosmology Telescope: Lensing of CMB Temperature and Polarization Derived from Cosmic Infrared Background Cross-correlation. 2015, ApJ, 808, 7, [arXiv:1412.0626](#)
- Zaldarriaga, M. & Seljak, U., Gravitational lensing effect on cosmic microwave background polarization. 1998, Phys. Rev. D, 58, 023003, [arXiv:astro-ph/9803150](#)
- ¹ APC, AstroParticule et Cosmologie, Université Paris Diderot, CNRS/IN2P3, CEA/Irfu, Observatoire de Paris, Sorbonne Paris Cité, 10, rue Alice Domon et Léonie Duquet, 75205 Paris Cedex 13, France
- ² Aalto University Metsähovi Radio Observatory and Dept of Radio Science and Engineering, P.O. Box 13000, FI-00076 AALTO, Finland
- ³ African Institute for Mathematical Sciences, 6-8 Melrose Road, Muizenberg, Cape Town, South Africa
- ⁴ Agenzia Spaziale Italiana Science Data Center, Via del Politecnico snc, 00133, Roma, Italy
- ⁵ Aix Marseille Université, CNRS, LAM (Laboratoire d'Astrophysique de Marseille) UMR 7326, 13388, Marseille, France
- ⁶ Astrophysics Group, Cavendish Laboratory, University of Cambridge, J J Thomson Avenue, Cambridge CB3 0HE, U.K.
- ⁷ Astrophysics & Cosmology Research Unit, School of Mathematics, Statistics & Computer Science, University of KwaZulu-Natal, Westville Campus, Private Bag X54001, Durban 4000, South Africa
- ⁸ CGEE, SCS Qd 9, Lote C, Torre C, 4° andar, Ed. Parque Cidade Corporate, CEP 70308-200, Brasília, DF, Brazil
- ⁹ CITA, University of Toronto, 60 St. George St., Toronto, ON M5S 3H8, Canada
- ¹⁰ CNRS, IRAP, 9 Av. colonel Roche, BP 44346, F-31028 Toulouse cedex 4, France
- ¹¹ CRANN, Trinity College, Dublin, Ireland
- ¹² California Institute of Technology, Pasadena, California, U.S.A.
- ¹³ Centro de Estudios de Física del Cosmos de Aragón (CEFCA), Plaza San Juan, 1, planta 2, E-44001, Teruel, Spain
- ¹⁴ Computational Cosmology Center, Lawrence Berkeley National Laboratory, Berkeley, California, U.S.A.
- ¹⁵ DSM/Irfu/SPP, CEA-Saclay, F-91191 Gif-sur-Yvette Cedex, France
- ¹⁶ DTU Space, National Space Institute, Technical University of Denmark, Elektrovej 327, DK-2800 Kgs. Lyngby, Denmark
- ¹⁷ Département de Physique Théorique, Université de Genève, 24, Quai E. Ansermet, 1211 Genève 4, Switzerland
- ¹⁸ Departamento de Astrofísica, Universidad de La Laguna (ULL), E-38206 La Laguna, Tenerife, Spain
- ¹⁹ Departamento de Física, Universidad de Oviedo, Avda. Calvo Sotelo s/n, Oviedo, Spain
- ²⁰ Department of Astronomy and Astrophysics, University of Toronto, 50 Saint George Street, Toronto, Ontario, Canada
- ²¹ Department of Astrophysics/IMAPP, Radboud University Nijmegen, P.O. Box 9010, 6500 GL Nijmegen, The Netherlands
- ²² Department of Physics & Astronomy, University of British Columbia, 6224 Agricultural Road, Vancouver, British Columbia, Canada
- ²³ Department of Physics and Astronomy, Dana and David Dornsife College of Letter, Arts and Sciences, University of Southern California, Los Angeles, CA 90089, U.S.A.
- ²⁴ Department of Physics and Astronomy, University College London, London WC1E 6BT, U.K.
- ²⁵ Department of Physics, Gustaf Hållströmin katu 2a, University of Helsinki, Helsinki, Finland
- ²⁶ Department of Physics, Princeton University, Princeton, New Jersey, U.S.A.
- ²⁷ Department of Physics, University of California, One Shields Avenue, Davis, California, U.S.A.
- ²⁸ Department of Physics, University of California, Santa Barbara, California, U.S.A.
- ²⁹ Department of Physics, University of Illinois at Urbana-Champaign, 1110 West Green Street, Urbana, Illinois, U.S.A.
- ³⁰ Dipartimento di Fisica e Astronomia G. Galilei, Università degli Studi di Padova, via Marzolo 8, 35131 Padova, Italy
- ³¹ Dipartimento di Fisica e Scienze della Terra, Università di Ferrara, Via Saragat 1, 44122 Ferrara, Italy
- ³² Dipartimento di Fisica, Università La Sapienza, P. le A. Moro 2, Roma, Italy
- ³³ Dipartimento di Fisica, Università degli Studi di Milano, Via Celoria, 16, Milano, Italy
- ³⁴ Dipartimento di Matematica, Università di Roma Tor Vergata, Via della Ricerca Scientifica, 1, Roma, Italy
- ³⁵ Discovery Center, Niels Bohr Institute, Blegdamsvej 17, Copenhagen, Denmark
- ³⁶ Discovery Center, Niels Bohr Institute, Copenhagen University, Blegdamsvej 17, Copenhagen, Denmark

- ³⁷ European Space Agency, ESAC, Planck Science Office, Camino bajo del Castillo, s/n, Urbanización Villafranca del Castillo, Villanueva de la Cañada, Madrid, Spain
- ³⁸ European Space Agency, ESTEC, Keplerlaan 1, 2201 AZ Noordwijk, The Netherlands
- ³⁹ Facoltà di Ingegneria, Università degli Studi e-Campus, Via Isimbardi 10, Novedrate (CO), 22060, Italy
- ⁴⁰ Gran Sasso Science Institute, INFN, viale F. Crispi 7, 67100 L'Aquila, Italy
- ⁴¹ HGSFP and University of Heidelberg, Theoretical Physics Department, Philosophenweg 16, 69120, Heidelberg, Germany
- ⁴² Helsinki Institute of Physics, Gustaf Hållströmin katu 2, University of Helsinki, Helsinki, Finland
- ⁴³ INAF - Osservatorio Astronomico di Padova, Vicolo dell'Osservatorio 5, Padova, Italy
- ⁴⁴ INAF - Osservatorio Astronomico di Roma, via di Frascati 33, Monte Porzio Catone, Italy
- ⁴⁵ INAF - Osservatorio Astronomico di Trieste, Via G.B. Tiepolo 11, Trieste, Italy
- ⁴⁶ INAF/IASF Bologna, Via Gobetti 101, Bologna, Italy
- ⁴⁷ INAF/IASF Milano, Via E. Bassini 15, Milano, Italy
- ⁴⁸ INFN, Sezione di Bologna, Via Imerio 46, I-40126, Bologna, Italy
- ⁴⁹ INFN, Sezione di Roma 1, Università di Roma Sapienza, Piazzale Aldo Moro 2, 00185, Roma, Italy
- ⁵⁰ INFN, Sezione di Roma 2, Università di Roma Tor Vergata, Via della Ricerca Scientifica, 1, Roma, Italy
- ⁵¹ IUCAA, Post Bag 4, Ganeshkhind, Pune University Campus, Pune 411 007, India
- ⁵² Imperial College London, Astrophysics group, Blackett Laboratory, Prince Consort Road, London, SW7 2AZ, U.K.
- ⁵³ Infrared Processing and Analysis Center, California Institute of Technology, Pasadena, CA 91125, U.S.A.
- ⁵⁴ Institut d'Astrophysique Spatiale, CNRS (UMR8617) Université Paris-Sud 11, Bâtiment 121, Orsay, France
- ⁵⁵ Institut d'Astrophysique de Paris, CNRS (UMR7095), 98 bis Boulevard Arago, F-75014, Paris, France
- ⁵⁶ Institute of Astronomy, University of Cambridge, Madingley Road, Cambridge CB3 0HA, U.K.
- ⁵⁷ Institute of Theoretical Astrophysics, University of Oslo, Blindern, Oslo, Norway
- ⁵⁸ Instituto de Astrofísica de Canarias, C/Vía Láctea s/n, La Laguna, Tenerife, Spain
- ⁵⁹ Instituto de Física de Cantabria (CSIC-Universidad de Cantabria), Avda. de los Castros s/n, Santander, Spain
- ⁶⁰ Istituto Nazionale di Fisica Nucleare, Sezione di Padova, via Marzolo 8, I-35131 Padova, Italy
- ⁶¹ Jet Propulsion Laboratory, California Institute of Technology, 4800 Oak Grove Drive, Pasadena, California, U.S.A.
- ⁶² Jodrell Bank Centre for Astrophysics, Alan Turing Building, School of Physics and Astronomy, The University of Manchester, Oxford Road, Manchester, M13 9PL, U.K.
- ⁶³ Kavli Institute for Cosmological Physics, University of Chicago, Chicago, IL 60637, USA
- ⁶⁴ Kavli Institute for Cosmology Cambridge, Madingley Road, Cambridge, CB3 0HA, U.K.
- ⁶⁵ Kazan Federal University, 18 Kremlyovskaya St., Kazan, 420008, Russia
- ⁶⁶ LAL, Université Paris-Sud, CNRS/IN2P3, Orsay, France
- ⁶⁷ LERMA, CNRS, Observatoire de Paris, 61 Avenue de l'Observatoire, Paris, France
- ⁶⁸ Laboratoire AIM, IRFU/Service d'Astrophysique - CEA/DSM - CNRS - Université Paris Diderot, Bât. 709, CEA-Saclay, F-91191 Gif-sur-Yvette Cedex, France
- ⁶⁹ Laboratoire Traitement et Communication de l'Information, CNRS (UMR 5141) and Télécom ParisTech, 46 rue Barrault F-75634 Paris Cedex 13, France
- ⁷⁰ Laboratoire de Physique Subatomique et Cosmologie, Université Grenoble-Alpes, CNRS/IN2P3, 53, rue des Martyrs, 38026 Grenoble Cedex, France
- ⁷¹ Laboratoire de Physique Théorique, Université Paris-Sud 11 & CNRS, Bâtiment 210, 91405 Orsay, France
- ⁷² Lawrence Berkeley National Laboratory, Berkeley, California, U.S.A.
- ⁷³ Lebedev Physical Institute of the Russian Academy of Sciences, Astro Space Centre, 84/32 Profsoyuznaya st., Moscow, GSP-7, 117997, Russia
- ⁷⁴ Max-Planck-Institut für Astrophysik, Karl-Schwarzschild-Str. 1, 85741 Garching, Germany
- ⁷⁵ National University of Ireland, Department of Experimental Physics, Maynooth, Co. Kildare, Ireland
- ⁷⁶ Nicolaus Copernicus Astronomical Center, Bartycka 18, 00-716 Warsaw, Poland
- ⁷⁷ Niels Bohr Institute, Blegdamsvej 17, Copenhagen, Denmark
- ⁷⁸ Niels Bohr Institute, Copenhagen University, Blegdamsvej 17, Copenhagen, Denmark
- ⁷⁹ Nordita (Nordic Institute for Theoretical Physics), Roslagstullsbacken 23, SE-106 91 Stockholm, Sweden
- ⁸⁰ Optical Science Laboratory, University College London, Gower Street, London, U.K.
- ⁸¹ SISSA, Astrophysics Sector, via Bonomea 265, 34136, Trieste, Italy
- ⁸² School of Physics and Astronomy, Cardiff University, Queens Buildings, The Parade, Cardiff, CF24 3AA, U.K.
- ⁸³ School of Physics and Astronomy, University of Nottingham, Nottingham NG7 2RD, U.K.
- ⁸⁴ Sorbonne Université-UPMC, UMR7095, Institut d'Astrophysique de Paris, 98 bis Boulevard Arago, F-75014, Paris, France
- ⁸⁵ Space Research Institute (IKI), Russian Academy of Sciences, Profsoyuznaya Str, 84/32, Moscow, 117997, Russia
- ⁸⁶ Space Sciences Laboratory, University of California, Berkeley, California, U.S.A.
- ⁸⁷ Special Astrophysical Observatory, Russian Academy of Sciences, Nizhnij Arkhyz, Zelenchukskiy region, Karachai-Cherkessian Republic, 369167, Russia
- ⁸⁸ Sub-Department of Astrophysics, University of Oxford, Keble Road, Oxford OX1 3RH, U.K.
- ⁸⁹ The Oskar Klein Centre for Cosmoparticle Physics, Department of Physics, Stockholm University, AlbaNova, SE-106 91 Stockholm, Sweden
- ⁹⁰ UPMC Univ Paris 06, UMR7095, 98 bis Boulevard Arago, F-75014, Paris, France
- ⁹¹ Université de Toulouse, UPS-OMP, IRAP, F-31028 Toulouse cedex 4, France
- ⁹² University of Granada, Departamento de Física Teórica y del Cosmos, Facultad de Ciencias, Granada, Spain
- ⁹³ University of Granada, Instituto Carlos I de Física Teórica y Computacional, Granada, Spain
- ⁹⁴ Warsaw University Observatory, Aleje Ujazdowskie 4, 00-478 Warszawa, Poland